Two-Chord Digital Holographic Interferometry on Sheared-Flow-Stabilized Z-Pinch Plasma

Zhangsheng Lian

A thesis
submitted in partial fulfillment of the
requirements for the degree of

Master of Science

University of Washington

2023

Committee:

Uri Shumlak

Justin Little

Program Authorized to Offer Degree:
Aeronautics & Astronautics

University of Washington

Abstract

Two-Chord Digital Holographic Interferometry
on Sheared-Flow-Stabilized Z-Pinch Plasma

Zhangsheng Lian

Chair of the Supervisory Committee:
Uri Shumlak
Department of Aeronautics & Astronautics

A two-chord digital holographic interferometry (DHI) setup is implemented on the ZaP-HD sheared-flow-stabilized (SFS) Z-pinch device. The SFS Z-pinch concept can potentially work as a fusion power generator or a space propulsion engine. The expanded DHI setup, combined with other diagnostics, offers a broader view about the plasma's structural evolution in the Z pinch. Two-dimensional instantaneous electron density profiles are measured from the DHI setup. Comparisons are made with pinch current centroid estimated from magnetic probe array. Field of view limitations and signal noise of the DHI setup are discussed. Suggestions are made to improve the capability of the DHI setup.

TABLE OF CONTENTS

LIST OF FIGURES

LIST OF TABLES

ACKNOWLEDGMENTS

I would like to thank prof. Uri Shumlak for guiding me into the realm of plasma, offering research opportunity, and providing mentorship with patience. It is my honor to work with this wise adviser. I will miss the stories he shared with us about scientific endeavour and life. I would like to thank prof. Justin Little for being part of the committee and the fun time in plasma classes. I would like thank Aqil Khairi, Harry Furey-Soper, Jeff Peachman, Jared Smythe, Bennett Diamond, Shane Murray, Nicolas Castriotta, and other students in the lab for creating a supportive and friendly environment, for fixing technical issues together, for helping out with run campaign, and for chatting about random topics. Special thanks to Aqil in keeping the lab running and fixing random problems that popped up. I would also like to thank Dr. Michael Ross and Dr. Eleanor Forbes for answering my questions about DHI and offering suggestions. I would like to thank Dr. Tobin Weber for helping out with PLC. Thank to my family for all love and the support in this academic journey. And thank to my friends for sharing their stories.

Chapter 1

INTRODUCTION

Controlled nuclear fusion has the potential to offer clean energy in vast quantities and may enable crewed interstellar travel. Fusion reactions occur when light nuclei fuse into heavy nuclei. Certain amount of energy is released from a fusion reaction, depending on the binding energy of reactant nuclei and product nuclei.

The most promising fusion fuels are deuterium and tritium, isotopes of hydrogen. On Earth, a small yet big enough fraction of water molecules have their hydrogen-1 atoms replaced by deuterium atoms, making deuterium widely available for extraction. Tritium is rare, but can be produced when energetic neutrons hit some lithium isotope, a process called tritium breeding. A small amount of deuterium and tritium can release plenty of fusion energy. Deuterium and tritium can power human civilization with clean energy far into the future. Deuterium can also be found in gas giants, making this fuel widely available within and beyond the solar system [1]. Deuterium-tritium (D-T) fusion can be achieved relatively easily, comparing to other fusion reactions. More details about fusion reactions are described in the following sections.

In rocket propulsion, specific impulse is a key performance measure. Specific impulse can be equivalently described by effective exhaust velocity. Effective exhaust velocity measures the impulse gained by a vehicle per unit mass of plume exhausted. An important characterization of a space mission is its delta-v requirement. Delta-v is the cumulative change in speed of a spacecraft. The rocket equation suggests that the required mass of a spacecraft increases exponentially with delta-v requirement, because its rocket has to propel both the remaining propellant and the rest of the spacecraft. The rocket equation also suggests that high effective exhaust velocity can significantly reduce the required mass for a spacecraft to

meet the delta-v requirement of a mission. Effective exhaust velocity is strongly related to the amount of kinetic energy contained per unit mass of plume. Fusion rocket promises both high effective exhaust velocity and decent thrust-to-weight ratio [2]. The superior performance of fusion rocket opens the possibility for deep-space spacecrafts to have a moderate total mass and to complete its mission in a reasonable time frame. Fusion rocket is a fair choice for deep space missions and potentially crewed missions beyond solar system.

1.1 Fusion Power

Unlike fission, where heavy nuclei spilt into light nuclei, fusion power has no risk of meltdown. In fission power, fission fuel undergoes self-sustaining chain reaction and requires deliberate effort to prevent fission fuel from reacting too fast. However, in fusion power, it takes deliberate effort to confine fusion fuel to make fusion reactions happen.

Certain nuclear reactions are of research interest for fusion power because they release a large amount of energy and have reasonably large reactivity or cross-section. D-T fusion has a relatively large reactivity at a relatively low temperature:

$$\mathrm{D} + \mathrm{T} \longrightarrow \mathrm{He}^4(3.5\,\mathrm{MeV}) + \mathrm{n}(14.1\,\mathrm{MeV}). \tag{1.1}$$

Nuclei have to be in close contact to make fusion reactions happen at all. However, all nuclei are positively charged, so their electrostatic forces tend to push them apart. Nuclei have to be confined in extreme temperature to overcome the said electrostatic forces. For example, D-T fusion has a reactivity $\langle \sigma\nu \rangle$ of about 4.2×10^{-16} cm^3/sec at 20 keV temperature [3]. To make fusion happen at some appreciable average power, it is also important to confine nuclei at sufficiently high density for a sufficiently long period of time. Temperature, density, and confinement time are three key parameters of fusion confinement.

Fusion reaction produces energetic particles. Some of these particles can impact structures inside a fusion reactor making those material radioactive. These activated materials must be managed as radioactive waste. Comparing to fission power, this is not a disadvantage, because spent fission fuel is a more challenging radioactive waste to manage [4].

1.2 Magnetic Confinement and Z pinch

A major focus of fusion research is to use electromagnetic forces to confine fusion fuel. Fusion fuel at fusion conditions is so hot that it exists as plasma. Plasma is conveniently susceptible to long-ranged electromagnetic forces. There are different approaches of magnetic confinement. The most famous approach is the tokamak, where the plasma is confined in a toroidal geometry, and magnetic fields are in both toroidal and poloidal directions.

The Z pinch is one of the oldest magnetic confinement concepts. Z-pinch plasma have a simple cylindrical geometry. Large electric current runs in the axial direction of the cylinder, usually from discharge of high voltage capacitors, as shown in Fig. 1.1. By Ampère's law, a magnetic field runs in the azimuthal direction of the cylinder. The balance between magnetic force and pressure is described by the Bennett relation in cylindrical form

$$\frac{d}{dr}\left(p + \frac{B_\theta^2}{2\mu_0}\right) = \frac{B_\theta^2}{\mu_0 r}, \tag{1.2}$$

where $\frac{B_\theta^2}{2\mu_0}$ is magnetic pressure and $\frac{B_\theta^2}{\mu_0 r}$ is magnetic tension [5].

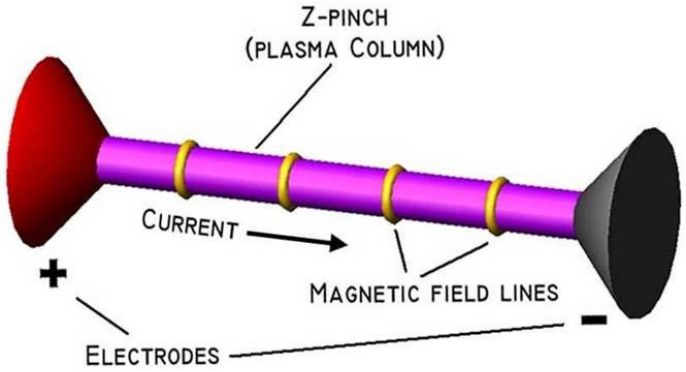

Figure 1.1: A diagram of Z pinch. Current flows on the axis from one electrode to the other. Magnetic field in azimuthal direction is generated by the current. [6].

1.3 Instablity in Z pinch

Early research on Z pinches revealed that they are plagued by instabilities. Some small perturbation of the pinch can quickly distort the entire pinch structure and end the confinement.

In $m = 0$ "sausage" mode instability, a region of the pinch starts slightly thinner than other region, resulting in a local increase in current density and magnetic field. Thus, the thinner region shrinks more rapidly due to the increased magnetic field, which eventually cuts the current flow.

In $m = 1$ "kink" mode instability, the pinch starts to bend off the axis slightly. One side of the pinch gains a stronger magnetic field than the other side. The imbalance in B-field bends the pinch further away from the axis. Two modes are shown in Fig. 1.2 below.

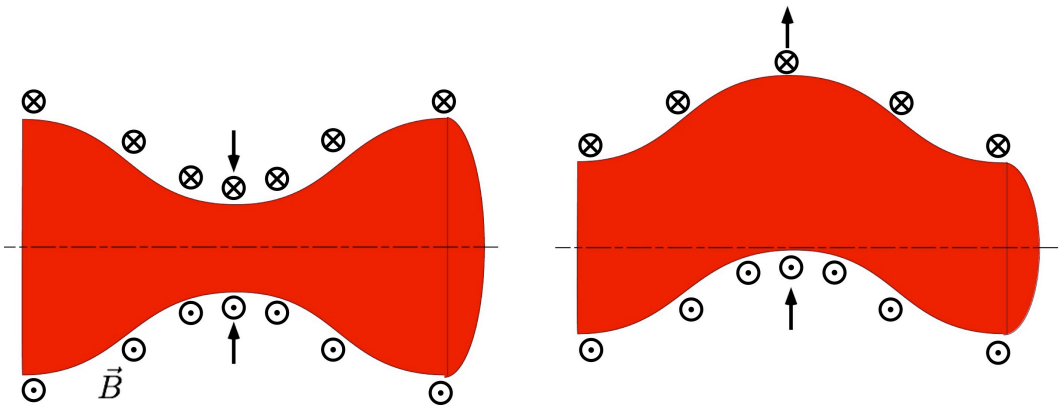

Figure 1.2: Left diagram shows $m = 0$ "sausage" mode, where a small thinning in the pinch can constrict the pinch even further. Right diagram shows $m = 1$ "kink" mode, where a small bend in the pinch can push the pinch to bend even further.

Different methods have been proposed to address this stability problem in Z pinches. Kadomtsev showed that $m = 0$ mode can be stabilized by having a gradual pressure distribution [7].

To better understand plasma confinement, knowledge about the distribution of plasma

particles is required. Density distribution measurements on the pinch provides information about the shape of the pinch. A shape that deviates from a column shows some form of instability in the plasma. Density measurement might also provide information about maximum density. Maximum density shows whether the plasma is tightly confined in order to approach fusion conditions.

Digital holographic interferometry (DHI) setup at ZaP-HD can measure spatially resolved density of the pinch over some area at an instant of time. DHI provides a good picture about the shape of the pinch and where the maximum density is. DHI can also to applied to other magnetic confinement configurations where plasma is dense enough to be measured with.

1.4 Sheared-Flow-Stabilized Z pinch

It was proposed by Uri Shumlak that sheared flow can be used to stabilize the $m = 1$ mode of Z pinches. The Z-pinch plasma can be thought of as concentric shells. The sheared shells must travel fast enough with respect to each other to suppress the $m = 1$ mode. The stability criterion is approximately

$$\frac{dv_z}{dr} \geq 0.1kV_A^0, \tag{1.3}$$

where v_z is axial flow velocity, k is axial wave number, and V_A^0 is the Alfvén speed ($V_A = B_\theta/\sqrt{\mu_0\rho}$) at maximum magnetic field and maximum plasma density [8].

Several sheared-flow-stabilized (SFS) Z-pinch devices have been built to test and verify this concept, with somewhat different geometry and increasing capacitor energy going to the plasma. All of them use coaxial electrodes to form sheared flow and compress Z pinch. Electrode layout of ZaP-HD is described in details in the following section. These devices exhibit an increasing trend in plasma temperature and density. A quick summary of these devices are shown in Table 1.1.

The first device, ZaP, demonstrated that its plasma remains stable significantly longer than a static Z pinch. ZaP includes two electrodes that are responsible for both forming the sheared flow and compressing the Z pinch. ZaP has relatively low plasma temperature

[9, 10].

The second device, ZaP-HD, has a higher plasma temperature and density. More details about this device are described in the following section.

The third device, FuZE, further increases plasma temperature, operating with two electrodes. Neutron emission from thermonuclear reaction was detected in FuZE [11]. The quiescent period of these Z-pinch devices are about 50 µs.

Table 1.1: Selected Parameters of SFS Z-pinch Devices [9, 10, 12, 6, 11, 13, 14, 15]

	ZaP	**ZaP-HD**	**FuZE**
Number of electrodes	2	3	2
Quiescent pinch current	$\sim$ 75 kA	$\sim$ 150 kA	$\sim$ 200 kA
Electron temperature	$\sim$ 75 eV	$\sim$ 1 keV	1-2 keV
Electron density	$\sim 2\times10^{22}$ m^{-3}	$\sim 2\times10^{23}$ m^{-3}	$\sim 10^{23}$ m^{-3}
Pinch radius	$\sim$ 1 cm	$\sim$ 0.3 cm	$\sim$ 0.3 cm

1.5 ZaP-HD Z-pinch Device

ZaP-HD is the second device built to test the sheared-flow-stabilized Z-pinch concept. Plasma can be compressed to higher density and pressure comparing to ZaP [5]. ZaP-HD's vacuum chamber can be divided into acceleration region, assembly region, and extension region. There are three coaxial electrodes in the vacuum chamber, as shown in Fig. 1.3. Inner and middle electrodes are used in the acceleration region and powered by acceleration capacitor banks. Inner and outer electrodes are used in the assembly region and powered by compression capacitor banks. The inner electrode ends with a tapered feature called nosecone, where it tends to get bombarded by energetic ions. The extension region is mounted after the assembly region and contains no electrode, shown in Fig. 1.4.

The vacuum chamber has multiple viewing ports for plasma diagnostics to view at different directions. Most importantly, there are four large rectangular windows on the assembly

region.

Note that the coordinate system of the device originates approximately at the tip of the nosecone. Positive z-direction is defined as the downstream direction from the origin. Positive y-direction is the vertical upward direction. X-direction is defined with right-handed coordinates. Under this coordinate system, for example, P10 denotes 10 cm downstream from the nosecone.

The vacuum chamber is pumped down by three stages of vacuum pumps: a turbopump, a roots blower and a rotary vane pump. Typical background pressure of the chamber is about 10^{-8} to 10^{-6} Torr.

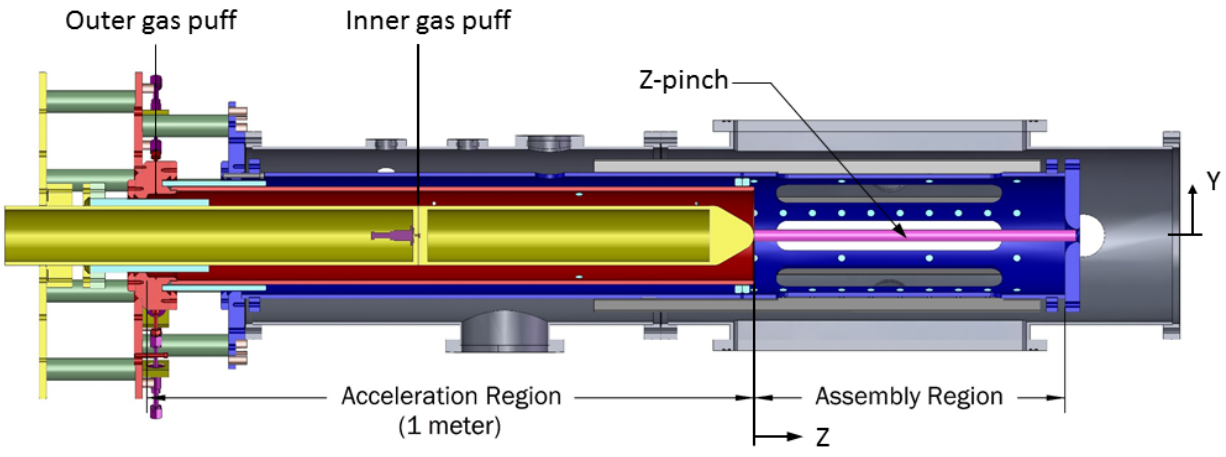

Figure 1.3: ZaP-HD Z-pinch Device's vacuum chamber (without extension in this figure) has three electrodes, shown here in yellow, red, and blue. Inner and middle electrodes are used in the acceleration region. Inner and outer electrodes are used in the assembly region [16].

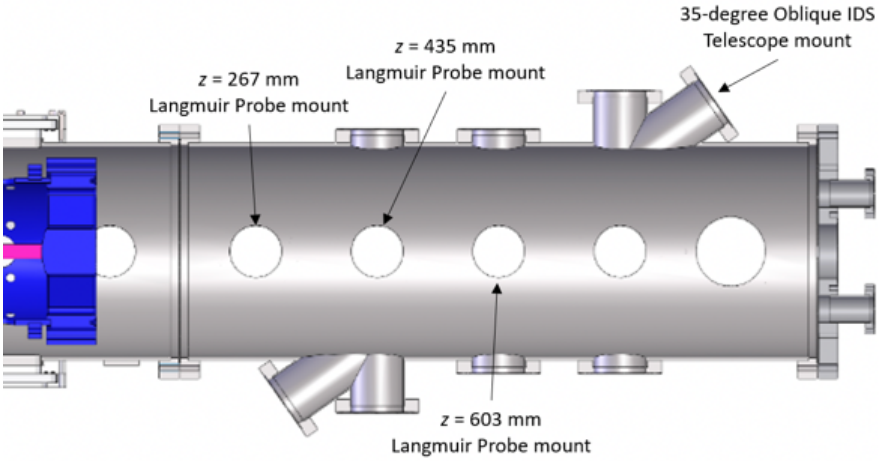

Figure 1.4: Extension region of ZaP-HD. The extension contains no electrode and is used to observe plasma plume resulted from the device [17].

The process of pinch formation is shown in Fig. 1.5. First, neutral gas is injected into the acceleration region. At around inner T+2 µs, the inner and middle electrodes discharge against the gas. The gas is ionized into plasma. Current flows from the middle electrode, though the plasma, into inner electrode, creating a B-field between two electrodes and behind the plasma. The plasma is accelerated by the Lorentz force downstream into the assembly region.

In the assembly region, controlled by some set time delay, inner and outer electrodes discharge against the plasma. Acceleration capacitor banks and compression capacitor banks are triggered independently, allowing more control on timing of compression action. During compression, part of the plasma stays attached to the nosecone. The other part of the plasma moves further downstream with higher velocity, forming sheared layers. With large electric current, the plasma is then compressed into a Z pinch.

The extension serves as an extra volume to observe the behavior of plasma plume generated by the pinch. The extension region has some impact on the pinch performance, but not seriously detrimental [17]. A quick summary of key parameters of ZaP-HD is shown in

Table 1.2.

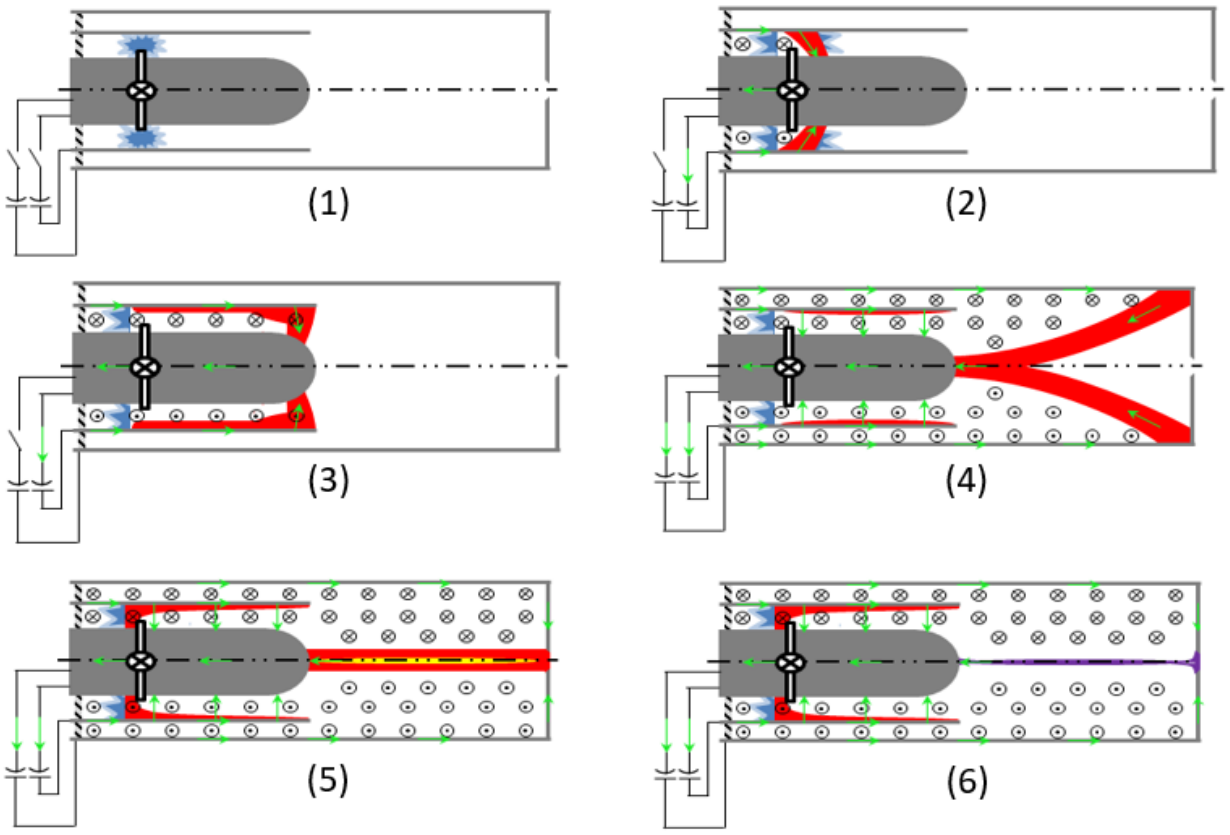

Figure 1.5: Neutral gas is injected in the acceleration region, where inner electrode and middle electrode discharges against the gas. The gas is ionized into plasma and accelerated towards assembly region. In the assembly region, outer electrode and inner electrode discharges against the plasma, creating Z pinch with sheared layers. [6].

Table 1.2: Key Parameters of ZaP-HD Z-pinch Device

	Value	**Notes**
Assembly region length	0.5 m	
Background Pressure	10^{-8}-10^{-6} Torr	
Acceleration capacitor voltage	9 kV	
Compression capacitor voltage	8 kV	
Maximum plasma current	$\sim$ 300 kA	
Maximum pinch current	$\sim$ 150 kA	[18]
Maximum ion temperature	$\sim$ 1 keV	[6]
Maximum electron density	$\sim 2\times10^{23}$ m^{-3}	
Pinch duration	$\sim$ 100 µs	
Quiescent period	$\sim$ 50 µs	[14]
Gas injected	H_2	most common
Mass of injected gas	$\sim$ 1 mg	

Chapter 2

OVERVIEW OF PLASMA DIAGNOSTICS ON ZAP-HD Z-PINCH EXPERIMENT

A suite of diagnostics is installed for ZaP-HD. The most utilized diagnostics are magnetic probes, Rogowski coils (current measurement), and voltage probes. These diagnostics provide important information about the basic operating status of the Z-pinch device. Spectroscopy devices on ZaP-HD observe line emission from energy transfer of bound electrons. Spectroscopy here mainly provides information about ion temperature and ion bulk velocity. Heterodyne quadrature interferometry with a He-Ne laser performs time-resolved electron density measurement at discrete locations of the plasma. Triple Langmuir probe on ZaP-HD mainly measures time-resolved electron temperature and electron density in the extension section. A high-speed imaging camera called Kirana is available to take a video of the plasma shot. Kirana can also work with spectrometers to perform time-resolved spectroscopy. Digital holographic interferometry (DHI) is able to measure electron density over some area at an instant. More details about DHI is discussed in the following chapters.

2.1 Magnetic Probe Array

Magnetic probes measure azimuthal magnetic fields in the vacuum chamber. Magnetic probes are placed in arrays in the chamber, as shown in Fig. 2.1. Each probe is a small soleoid coil, oriented to measure azimuthal field. It directly measures induced emf due to change in magnetic flux using Faraday's law:

$$V_{emf} = -\frac{d\Phi}{dt} = -nA\frac{dB}{dt}, \tag{2.1}$$

where n is coil winding count, and A is area of coil. The emf signal has to be integrated in order to proportionally represent the B-field. The probes were calibrated upon installation

to compensate for the image current produced by the surrounding metal [5].

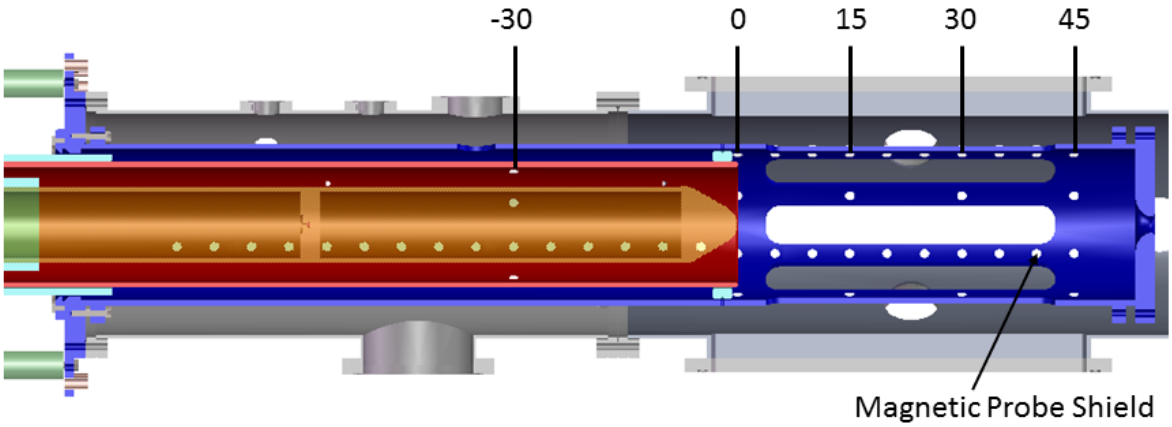

Figure 2.1: In the acceleration region, magnetic probes are attached to the middle electrode. In the assembly region, magnetic probes are attached to the outer electrode. Probes in the assembly region are arranged into azimuthal arrays of four or eight probes [5].

Modes of the B-field can be calculated at each azimuthal array. Fourier expansion is performed on the data collected by the array. The magnitude of a mode corresponds to some Fourier coefficient. The m = 1 mode data is particularly useful, indicating how the current centroid drifts away from the central axis. This quantifies the stability of the pinch. The radial displacement of pinch current away from the central axis is

$$\Delta r = \frac{1}{2}\frac{m_1}{m_0} r_{wall} \text{ [19].} \tag{2.2}$$

When the normalized m = 1 mode value $m_1/m_0 < 0.2$, the radial displacement of the current is less than 1 cm. Quiescent period is defined as the time when $m_1/m_0 < 0.2$ [5].

Magnetic probe data is also useful in monitoring capacitor discharge behaviors. Abnormal capacitor discharges can result in early or late change of magnetic curves.

2.2 Rogowski Coil

A Rogowski coil wraps around some current path to measure the amount of current passing through. A Rogowski coil works in a way similar to a magnetic probe. Change of current in the path induce some change in B-field, and this change in B-field induces some emf on the Rogowski coil. This emf signal can be integrated to reveal current strength.

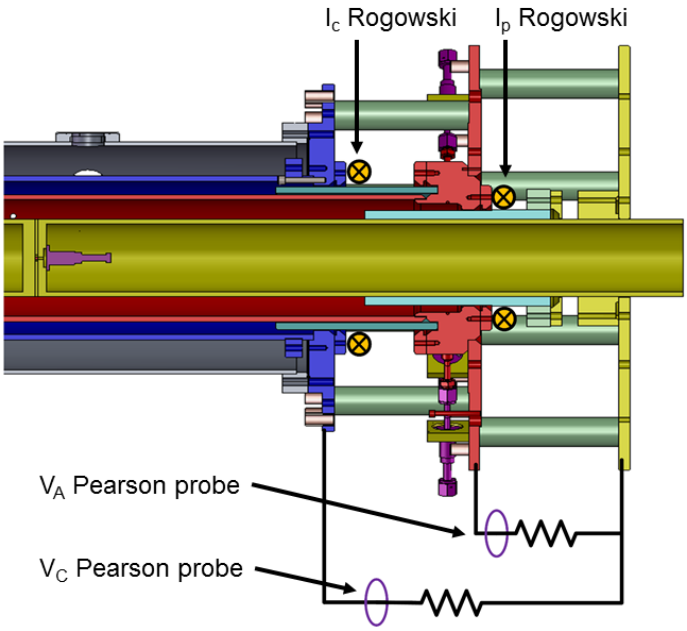

Figure 2.2: Rogowski coil and voltage measurement on ZaP-HD. I_C coil measures net current on inner (yellow) and middle (red) electrode, which usually equals current in outer (blue) electrode. I_P coil measures current of inner (yellow) electrode. Voltage probes measure voltage between electrode pairs [5].

There are three Rogowski coils wrapped around ignitrons monitoring current output by the capacitor banks. There are two coils wrapped around ZaP-HD electrodes, shown in Fig. 2.2. One coil measures net current on inner and middle electrode, which usually equals current in outer electrode. This current is called compression current (I_c) or pinch current. The other coil measures current of inner electrode. This current is called plasma current

(I_p).

Current measurement shows how much current is spent on creating sheared flow and how much current is flowing in the pinch. Current measurement is the main method to monitor how capacitor discharges into the vacuum chamber during daily operation of the Z pinch. Early or late rise in current can reveal abnormal capacitor behaviors.

In the last few months, it was observed that compression current measurement is abnormally low. We suspect that the configuration of I_c Rogowski coil might have been changed unintentionally. I_c Rogowski coil has to be recalibrated, and this thesis does not use data from I_c

2.3 Voltage Measurement

Voltage between ZaP-HD electrode pairs are measured by monitoring current travelling through some known resistors installed between electrode pairs. A schematic is shown in Fig. 2.2 above. Note that the outer (blue) electrode is always grounded. If this voltage measurement is assumed to have negligible impact on the overall circuit, then the middle (red) and inner (yellow) electrode are considered floating when there is no plasma.

Voltage measurement can be a supplement to current measurement in monitoring capacitor discharges. Voltage measurement provides key information about plasma disruption and possible arcing across insulating material in the vacuum chamber.

2.4 Spectroscopy

Spectroscopy is used to measure ion temperature and ion bulk velocity. Spectroscopy works by observing line emission from the plasma. When an electron jumps from high energy level to low energy level in an ion, light of some specific wavelength is emitted. The wavelength observed by spectroscopy devices depends on thermal speed of ions and bulk velocity of ions due to Doppler effect. Thermal speed tends to expand the wavelength profile, called Doppler broadening. Bulk velocity tends to shift the wavelength, called Doppler shift. To measure bulk velocity, a spectroscopy device has to collect light with a component parallel

to the direction of said velocity. In ZaP-HD, axial bulk velocity is of a major interest to understand sheared flow, so spectroscopy devices have the option to look at plasma from an oblique angle.

Hydrogen might be fully ionized in ZaP-HD, so no electron can emit line radiation from such hydrogen. Often, a spectroscopy device looks for line-emission from impurities, such as carbon and oxygen.

Common spectroscopy cameras like PI MAX 4 cannot take video near the speed of Z pinch. High-speed camera Kirana is used to take temporally resolved spectroscopy data over the pinch duration. More details about high-speed spectroscopy can be found in Eleanor Forbes's work [20].

2.5 Heterodyne Quadrature Interferometry

Heterodyne quadrature interferometry measures temporally resolved electron density at discrete locations in the plasma over the pinch duration. For basic theory about plasma interferometry, see Section 3.1. Heterodyne quadrature interferometry in ZaP-HD employs a He-Ne laser with a wavelength of 633 nm. The reference beam of the laser is brought to a slightly different frequency, 40 MHz away from the scene beam, by a Bragg Cell. This heterodyne of scene beam and reference beam has a low enough frequency to be detected by photo diodes. A schematic is shown in Fig. 2.3. Evolution of heterodyne phase is analyzed to reveal line-integrated electron density. Similar to DHI, Abel inversion can be performed on line-integrated electron density to estimate electron number density, by assuming some geometry of the plasma.

As mentioned before, density measurement is important in understanding the plasma confinement. Compared to the current DHI setup, heterodyne quadrature interferometry has temporal resolution over the entire pinch duration but limited spatial resolution. More details about ZaP-HD's heterodyne quadrature interferometry can be found in Sean D. Knecht's work and Michael Ross's dissertation [21, 5].

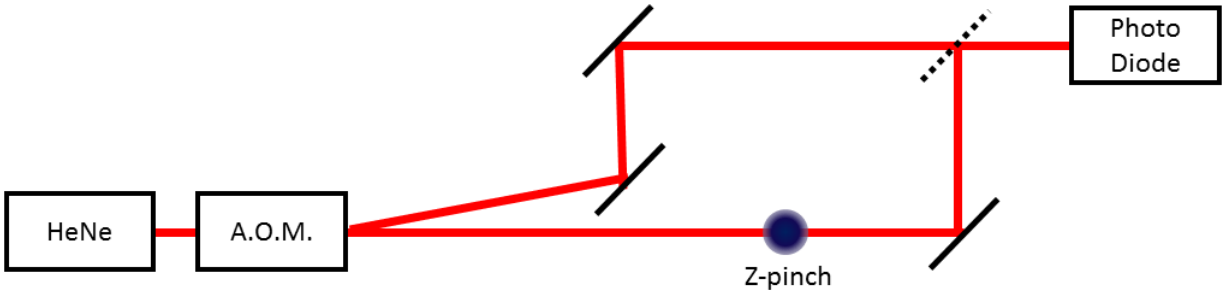

Figure 2.3: A Mach–Zehnder interferometry setup. The reference beam is set to a slightly different frequency than the scene beam by acousto-optic modulator (AOM, or Bragg Cell). The phase of scene beam is affected by the plasma. The two beams create a heterodyne on the photo diode. The heterodyne is recorded for analysis of electron density [21, 5].

2.6 Triple Langmuir Probe

A Langmuir probe is able to measure electron density and electron temperature. The probe has to be placed inside the plasma to make a measurement. Langmuir probe measurement relies on charged particles travelling through a sheath. A sheath is the region between bulk plasma and surface material, where some plasma ions travel to the surface. There are different theories that model the sheath. In single Langmuir probe, a variable biased voltage is applied on the probe tip. Current travelling through the probe tip is recorded, as biased voltage is adjusted. Data about biased voltage and corresponding current is then used to calculate electron density and electron temperature.

In a triple Langmuir probe, three probe tips are at different voltages. There is no need to use variable biased voltage. This eliminates the time required to scan over some biased voltage interval, offering a much higher temporal resolution than single probe. Current travelling through three probe tips are recorded, providing sufficient data to calculate electron density and electron temperature.

The Langmuir probe in ZaP-HD is used mainly to collect data in the extension region to study plume characteristics of the pinch. The plume characteristics can help us understand

performance of Z pinch as a rocket propulsion device and what can be done to maximize rocket performance. More details about ZaP-HD's Langmuir probe can be found in Jared Smythe's thesis [17].

2.7 High-speed Imaging

A high speed camera called Kirana is capable of taking video of the plasma mostly at visible wavelengths. Kirana can operate at a maximum speed of five million frames per second. Kirana can record at most 180 frames in a single plasma shot, due to data buffering limitations. Most of light recorded by Kirana comes from emission from neutral hydrogen. Video taken by Kirana gives a rough estimate about where the plasma is and can be used to analyze centroid and other geometric features of the plasma [22].

As mentioned previously, Kirana can also be used to perform temporally solved spectroscopy over the pinch duration.

Chapter 3

THEORY OF DIGITAL HOLOGRAPHIC INTERFEROMETRY

Different from an ordinary photo, a hologram includes information about phase of light. Holograms are usually produced with two laser beams, where the two beams generate some interference pattern. The ability to record phase information serves well for interferometry. Two holograms taken with and without plasma are used to calculate the phase shift caused by the plasma.

3.1 Interferometry on Plasma

Plasma interferometry measures electron density by examining phase of light. To observe the phase without ambiguity, a coherent light source is used, usually a laser. Comparing to light in vacuum, light in plasma can interact with charged particles and, for example, propagate at different phase velocity and wave number. First, assume that thermal velocity of plasma has no impact on light. Considering interaction with electron only, if the plasma frequency is much larger than electron cyclotron frequency, then such light wave can be approximated as an O wave with dispersion relation

$$n^2 = \left(\frac{c}{v_\phi}\right)^2 = \frac{c^2k^2}{\omega^2} = 1 - \frac{\omega_p^2}{\omega^2}, \tag{3.1}$$

where n is the refractive index of plasma, c is the speed of light, v_ϕ is the phase velocity of light, k is the angular wavenumber of light, ω is the angular temporal frequency of light, and ω_p is the plasma frequency [23].

Phase of coherent light is simply its wavenumber integrated over distance:

$$\phi = \int kdl = \int \frac{\omega}{c} ndl. \tag{3.2}$$

By comparing the phase of light affected by plasma and the phase of unaffected light, information about the refractive index of plasma can be extracted:

$$\Delta\phi = \int (k_{plasma} - k_0) dl = \int (n-1)\frac{\omega}{c} dl. \tag{3.3}$$

Refractive index of a plasma is related to the electron density by expanding the plasma frequency:

$$n^2 = 1 - \frac{\omega_p^2}{\omega^2} = 1 - \frac{n_e e^2}{\omega^2 m_e \epsilon_0} = 1 - \frac{n_e}{n_c}, \tag{3.4}$$

where n_e is electron density, m_e is electron mass, and n_c is the cutoff density. Laser frequency must be sufficiently high to allow O-waves to propagate in the plasma. Phase shift can then be related to electron density by:

$$\Delta\phi = \frac{\omega}{c} \int \left[\left(1 - \frac{n_e}{n_c}\right)^{1/2} - 1 \right] dl. \tag{3.5}$$

If laser frequency is high enough where $n_e \ll n_c$, then the refractive index can be approximated as

$$n = 1 - \frac{1}{2}\frac{n_e}{n_c}. \tag{3.6}$$

The phase shift has a simplified form directly proportional to integrated electron density:

$$\Delta\phi = -\frac{\omega}{2cn_c} \int n_e dl = -\frac{e^2}{2c\omega m_e \epsilon_0} \int n_e dl = -\frac{e^2}{4\pi c^2 m_e \epsilon_0} \lambda \int n_e dl, \tag{3.7}$$

where λ is the laser frequency [24].

3.2 Holographic Interferometry

Digital holographic interferometry in this experiment uses a Mach-Zehnder interferometer setup. The main laser beam is expanded in order to cover a large portion of camera sensor area. The main beam is split into a scene beam and a reference beam. The scene beam travels through the plasma, where its phase is manipulated. The reference beam does not

travel through the plasma. Both scene beam and reference beam are then directed to a camera sensor. A schematic is shown in Fig. 3.1.

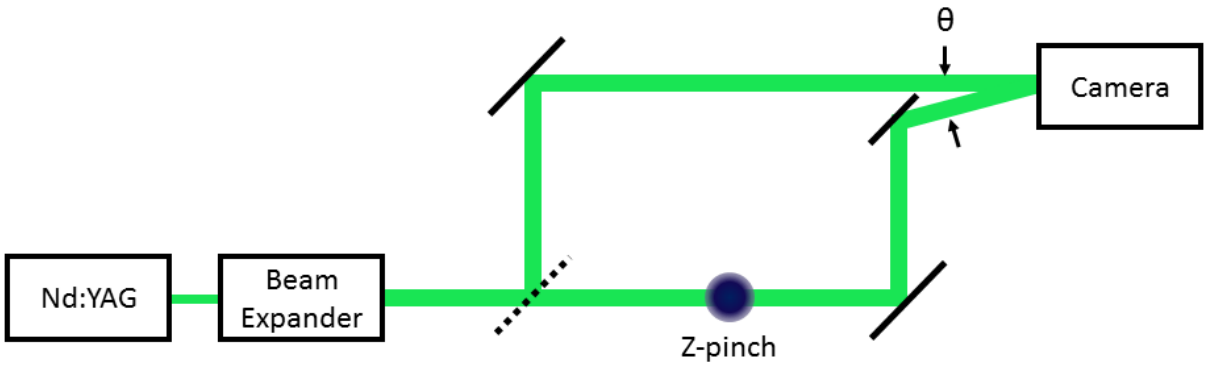

Figure 3.1: A schematic of the holographic interferometry setup. The laser beam is expanded to cover a large portion of of camera sensor area. The main laser beam is split into a scene beam and a reference beam. The scene beam interacts with the plasma. These two beams are slightly misaligned at some small angle θ, so that they reach different pixels on the camera sensor at different phase respectively, creating an interference pattern over the sensor [16].

Two beams are slightly misaligned at some small angle θ. Two beams travel different distance to reach the same pixel on camera sensor, so that two beam arrive at a pixel at different phases. The difference in travel distance is not constant over the sensor, due to the misalignment angle. Thus, phase shift of two beams is different at different pixels, creating interference pattern over the sensor. The fringe spacing δ is related to misalignment angle and laser wavelength by:

$$\delta = \frac{\lambda}{\sin\theta}. \tag{3.8}$$

By the Nyquist sampling criterion, there must be more than two pixels to properly sample the fringes. Fringe spacing must be sufficiently large compared to pixel size. Longer laser wavelength or smaller misalignment angle can increase fringe spacing [5].

To summarize the choice of laser wavelength, in order to use consumer cameras as detectors, the wavelength must be in the visible region so that the camera sensors can see the light. The wavelength has to be short enough so that light can propagate in dense plasma. The wavelength has to be somewhat long to increase fringe spacing. In this experiment, the second harmonic wavelength (532 nm) of Nd:YAG laser serves well.

3.3 Holographic Reconstruction

Once a hologram is collected by the camera, holographic reconstruction has to be performed to eventually reveal the phase information contained in the hologram. A hologram recorded by a film can be reconstructed by shining the reference beam on the film and capturing the diffracted light with a plate. The reconstruction plane collects diffracted light at some distance d away from the hologram, as shown in Fig. 3.2 With a digital camera, holographic reconstruction can be done by simulating diffraction numerically.

Light can be modelled by its electric field E. Incident beams are modelled as spherical waves emitted from point source for generality:

$$E_R = \frac{E_{0R}}{d_R} \exp[i(kd_R + \phi_R)] \tag{3.9}$$

$$E_S = \frac{E_{0S}}{d_S} \exp[i(kd_S + \phi_S)], \tag{3.10}$$

where E_{0R} and E_{0S} are wave amplitudes, d_R and d_S are the distances away from the beams' point sources, ϕ_R and ϕ_S are arbitrary initial phases. Intensity of light I is defined as

$$I = |E|^2. \tag{3.11}$$

The camera sensor is assumed to have a linear response to incident light, and some light intensity is not captured by the sensor. Transmittance $T(x, y)$ of a recorded hologram is a function of intensity and can be modeled by

$$T(x, y) = \alpha - \beta\tau I(x, y), \tag{3.12}$$

where α is a constant for uniform background illumination, β is sensor's light sensitivity, and τ is sensor's exposure time to the intensity $I(x, y)$. Intensity reaching the sensor is a sum of incident reference beam and scene beam, which can then be computed:

$$I(x, y) = E_S E_S^* + E_S E_R^* + E_R E_S^* + E_R E_R^*, \tag{3.13}$$

where * indicates the complex conjugate.

Holographic reconstruction is performed by passing reference beam on the hologram, which can be described mathematically by

$$E_{rec} = T E_R, \tag{3.14}$$

where E_{rec} is E-field of reconstructed light. Transmittance T can be expanded to reveal composition of E_{rec}:

$$\begin{aligned} E_{rec} = &- \beta\tau |E_R|^2 E_S \cdots \\ &- \beta\tau E_R^2 E_S^* \cdots \\ &+ (\alpha - \beta\tau(|E_R|^2 + |E_S|^2)) E_R. \end{aligned} \tag{3.15}$$

On the reconstruction plane, with enough reconstruction distance, three images would appear, each corresponding to a different term in E_{rec}. The first term ($\propto E_S$) is directly proportional to scene beam by some constant, and corresponds to first-order diffraction. The second term ($\propto E_R^2 E_S^*$), also a first-order diffraction, is a conjugate image of the first term. The third term ($\propto E_R$) corresponds to no diffraction. In practice, consider E_R as a plane wave. Thus, on the phase maps, the first-order terms are simply 180^o out of phase from each other, but they are otherwise identical. Two first-order images are called twin images. Camera sensor response is usually not linear, but this non-linearity does not affect the phase of first-order image [16].

In coding practice, recorded holograms are converted from color into grayscale related to the wavelength of the laser. A hyperbolic window is applied on the hologram to attenuate pixels near edges of the photos to reduce Gibbs phenomena in reconstruction [5].

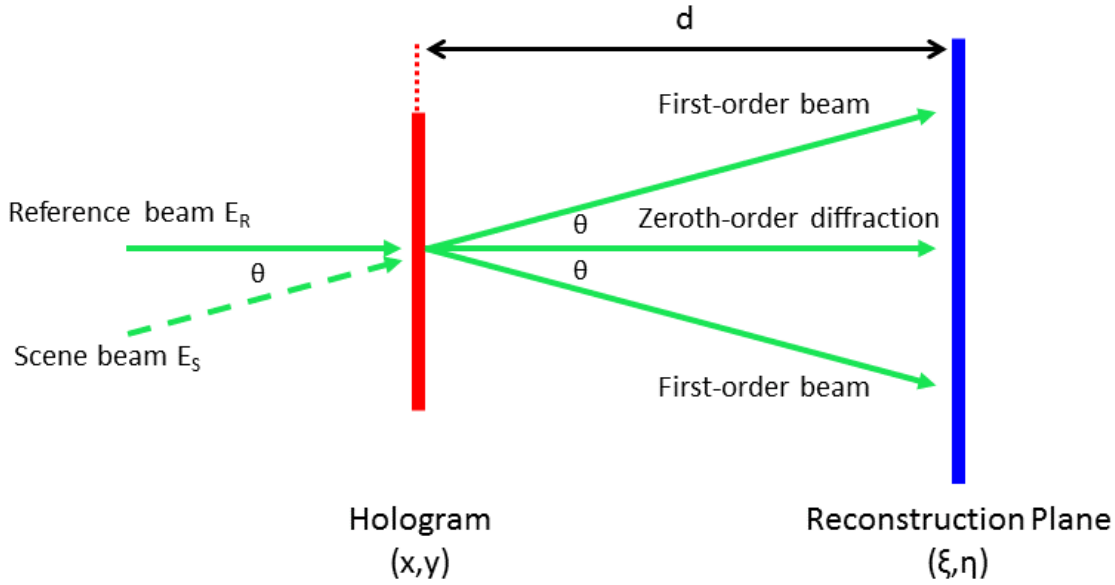

Figure 3.2: A diagram of holographic reconstruction. Reference beam is applied on the recorded hologram to cause diffraction, resulting in two first-order diffraction and one zeroth-order diffraction. A reconstruction distance d is selected so that first-order image and zeroth-order image would not overlap. The first-order image is closely related to phase of the scene beam. [16].

3.4 Fresnel Transform

This section presents a way to actually compute reconstruction. Diffraction here can be described by the Huygens-Fresnel principle. Huygens-Fresnel principle "posits that each point on an electromagnetic wavefront is a source of secondary spherical wavelets [16]." The E-field resulting from diffraction is a convolution of secondary wavelets and transmittance of the hologram:

$$E_{rec}(\xi,\eta) = \int_{-\infty}^{\infty}\int_{-\infty}^{\infty} h(\xi,\eta;x,y)T(x,y)dxdy, \tag{3.16}$$

where $h(\xi,\eta;x,y)$ is secondary wavelet, and $T(x,y)$ is transmittance of the hologram. The secondary wavelets can be modeled generally as spherical waves from point sources.

$$h(\xi,\eta;x,y) = \frac{1}{i\lambda}\frac{\exp(ik\rho)}{\rho}, \tag{3.17}$$

where ρ is the distance from point source. In principle, this convolution can be performed in Fourier space

$$E_{rec}(\xi,\eta) = \mathcal{F}^{-1}\{\mathcal{F}\{h(\xi,\eta;x,y)\}\mathcal{F}\{T(x,y)\}\}. \tag{3.18}$$

Instead, consider a secondary wavelet model simplified with parabolic wave as long as the reconstruction distance d is large compared to the size of the aperture

$$h(\xi,\eta;x,y) = \frac{\exp(ikd)}{i\lambda d}\exp\left(i\frac{k}{2d}[(x-\xi)^2+(y-\eta)^2]\right). \tag{3.19}$$

Inserting this secondary wavelet expression back to the convolution (Eq. 3.16),

$$E_{rec}(\xi,\eta) = \int_{-\infty}^{\infty}\int_{-\infty}^{\infty}\frac{\exp(ikd)}{i\lambda d}\exp\left(i\frac{k}{2d}[(x-\xi)^2+(y-\eta)^2]\right)T(x,y)dxdy, \tag{3.20}$$

$$\begin{aligned}E_{rec}(\xi,\eta) = {} & \frac{\exp(ikd)}{i\lambda d}\exp\left(i\frac{k}{2d}(\xi^2+\eta^2)\right) \\ & \int_{-\infty}^{\infty}\int_{-\infty}^{\infty}\exp\left(i\frac{k}{2d}(x^2+y^2)\right)\exp\left(-i\frac{k}{2d}2(x\eta+y\xi)\right)T(x,y)dxdy.\end{aligned} \tag{3.21}$$

With a change of variables

$$\nu = \frac{\xi}{d\lambda} \tag{3.22}$$

$$\mu = \frac{\eta}{d\lambda}, \tag{3.23}$$

the convolution can be further simplified

$$\begin{aligned}E_{rec}(\nu,\mu) = {} & \frac{\exp(ikd)}{i\lambda d}\exp\left(i\pi\lambda d(\nu^2+\mu^2)\right) \\ & \int_{-\infty}^{\infty}\int_{-\infty}^{\infty}\exp\left(\frac{i\pi}{d\lambda}(x^2+y^2)\right)\exp\left(-i2\pi(x\mu+y\nu)\right)T(x,y)dxdy.\end{aligned} \tag{3.24}$$

This is a Fourier transform

$$E_{rec}(\nu,\mu) = A\mathcal{F}\{\exp\left(\frac{i\pi}{d\lambda}(x^2+y^2)\right)T(x,y)\} = A\mathcal{F}\{C(x,y)T(x,y)\}, \tag{3.25}$$

where A is some coefficient that does not affect phase shift. This transform is called Fresnel transform.

In the reconstruction plane, pixels have the following size

$$\Delta\xi = \frac{d\lambda}{M\Delta x} \tag{3.26}$$

$$\Delta\eta = \frac{d\lambda}{N\Delta y}, \tag{3.27}$$

where $\Delta\xi$ and $\Delta\eta$ are pixel sizes on the reconstruction plane, M and N are pixel counts on the hologram, and Δx and Δy are pixel sizes on the sensor [25]. Therefore, the spatial size of the reconstruction plane is $d\lambda/\Delta x$ by $d\lambda/\Delta y$, which is usually a square. The zeroth-order and first-order images have the same size as the camera sensor. Location of first-order image can be estimated by

$$h_i = d\tan\left(\arcsin\frac{\lambda}{\delta}\right) = d\tan\theta, \tag{3.28}$$

where h_i is the distance from the center of the first-order image to the center of the reconstruction plane [16].

The reconstruction distance must be large enough to allow the first-order images to separate from the zeroth-order image. On the other hand, as the distance increases, pixel size on the reconstruction plane increases, and the pixel count of the first-order image becomes small. Therefore, the reconstruction distance should be kept reasonably small to allow more resolution on the first-order image. The misalignment angle should be appropriately small, so that there is no aliasing on the pixels and short reconstruction distance can be used [16].

In coding practice, Eq.3.25 is discretized. Some chirp function is created to fulfill the role of $C(x,y)$, and inverse Fast Fourier Transform (FFT) is used [6]. FFT shift is used to place the zero-frequency component in the center of the spectrum during inverse FFT.

3.5 Unwrapping Phase Information

Complex E-field on the reconstruction plane is calculated by Fresnel transform. Again first-order image on the reconstruction plane is directly proportional to the scene beam E-field. By comparing two holograms taken with and without plasma, phase shift between scene beams is calculated.

In general, phase of E-field on the reconstruction plane is

$$\phi(\xi,\eta) = \arctan\left(\frac{\operatorname{Im} E(\xi,\eta)}{\operatorname{Re} E(\xi,\eta)}\right). \tag{3.29}$$

The most obvious way to calculate phase difference is direct subtraction:

$$\Delta\phi(\xi,\eta) = \phi_p(\xi,\eta) - \phi_v(\xi,\eta), \tag{3.30}$$

where ϕ_p is phase of plasma hologram, ϕ_v is phase of baseline hologram. Alternatively, phase shift between two complex E-fields is simply the phase of their quotient:

$$\Delta\phi(\xi,\eta) = \arctan\left(\frac{\operatorname{Im}(E_p(\xi,\eta)/E_v(\xi,\eta))}{\operatorname{Re}(E_p(\xi,\eta)/E_v(\xi,\eta))}\right). \tag{3.31}$$

The quotient can be rewritten as

$$\frac{E_p(\xi,\eta)}{E_v(\xi,\eta)} = \frac{E_p(\xi,\eta)E_v^*(\xi,\eta)}{|E_v(\xi,\eta)|^2}. \tag{3.32}$$

The phase shift is then calculated by

$$\Delta\phi(\xi,\eta) = \arctan\left(\frac{\operatorname{Im}\left(\frac{E_p(\xi,\eta)E_v^*(\xi,\eta)}{|E_v(\xi,\eta)|^2}\right)}{\operatorname{Re}\left(\frac{E_p(\xi,\eta)E_v^*(\xi,\eta)}{|E_v(\xi,\eta)|^2}\right)}\right) = \arctan\left(\frac{\operatorname{Im}(E_p(\xi,\eta)E_v^*(\xi,\eta))}{\operatorname{Re}(E_p(\xi,\eta)E_v^*(\xi,\eta))}\right). \tag{3.33}$$

In coding, this computed phase shift is confined in some 2π interval. Some unwrapping algorithm has to be applied to unwrap the phase shift beyond any 2π interval. Before unwrapping, noise has to be smoothed, and discontinuous fringe jumps have to be preserved. Thus, sine and cosine of phase are smoothed independently, with boxcar smoothing algorithm. Limited by the boxcar smoothing, pixels near the edge of first-order image cannot be smoothed. After smoothing the signal, phase shift is computed again:

$$\Delta\phi_{smooth} = \arctan\left(\frac{(\sin\Delta\phi)_{smooth}}{(\cos\Delta\phi)_{smooth}}\right) [16]. \tag{3.34}$$

To unwrap the phase, noisy pixels near the edge must be trimmed, so that the unwrapping algorithm is not disturbed.

3.6 Abel Inversion

Phase shift provides information about line-integrated density. With practically one view, number density can only be estimated with some assumptions on the 3D density distribution of plasma. Usually, Z pinch is assumed to have concentric shells of uniforms density, best illustrated by Fig. 3.3.

A continuous form of Abel inversion is given by

$$N_e(y) = 2\int_y^\infty \frac{n_e(r)rdr}{\sqrt{r^2 - y^2}}, \tag{3.35}$$

where $N_e(y)$ is observed line-integrated density at distance y (impact parameter) away from pinch centroid, r is a variable radial distance to facilitate the integral. This continuous form can be discretized into a linear system of equations

$$\vec{N_e} = 2\Delta r \mathbf{A}\vec{n_e}, \tag{3.36}$$

where $\vec{N_e}$ is an array of line-integrated density across the pinch, Δr is the thickness of shells due to resolution of $\vec{N_e}$, and matrix $\mathbf{A}$ contains relative length that light travelled in different shells. $\vec{N_e}$ is a superposition of densities of shells. Density distribution $\vec{n_e}$ can be calculated by solving this linear system of equations.

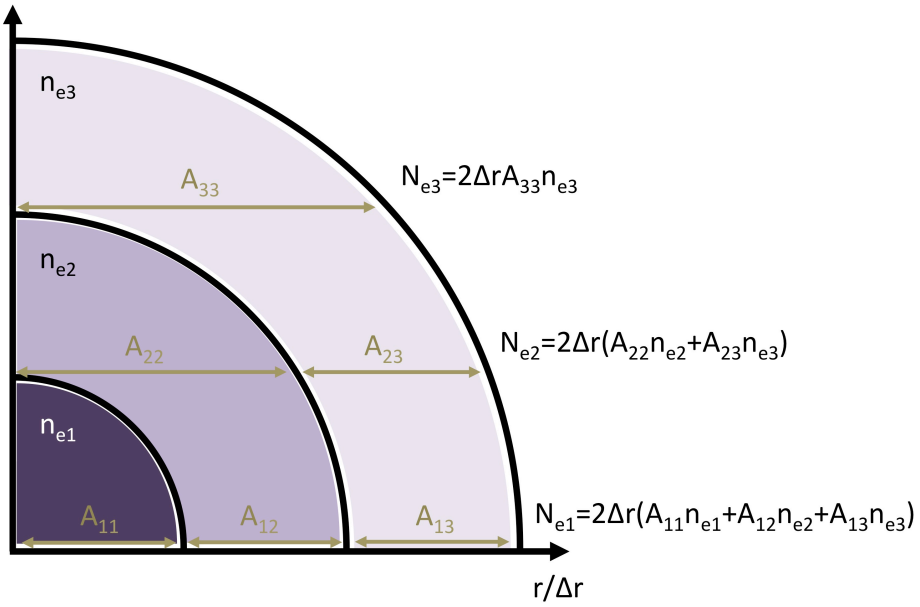

Figure 3.3: Discretized Abel inversion on Z-pinch density distribution. Z pinch is assumed to be made of concentric shells of uniform density. Resulting line-integrated density at a pixel is a superposition of the densities of these shells [5].

Reader can refer to Michael Ross's PhD dissertation for more details about theory of the DHI set implemented in ZaP-HD.

Chapter 4

EXPERIMENTAL SETUP OF DIGITAL HOLOGRAPHIC INTERFEROMETRY

Again, a schematic of the DHI setup is in Fig. 3.1. Laser beam is expanded by a beam expander to cover a wider area of the plasma and to cover a large portion of camera sensor area.

4.1 Laser Operation

Table 4.1: Selected NL121G-SH Nd:YAG Laser Performance Data

	Value	**Notes**
Beam diameter	$\sim$ 5 mm	Not a perfect circle due to SHG crystal heater out of order. Does not affect phase information on DHI. Can limit field of view of DHI.
Pulse duration at 1064 nm	1.9 ns	FWHM, tested in 2014
Maximum output energy at 532 nm	21.1 mJ RMS 1.5%	Measured by laser power meter in 2023

In the DHI setup, a Nd:YAG laser model NL121G-SH manufactured by EKSPLA is used. The fundamental wavelength of Nd:YAG laser is 1064 nm. The second harmonic wavelength, 532 nm, created by the second-harmonic generation (SHG) crystal in the laser unit, is used

for the experiment [26]. There is some small variation in laser performance from shot to shot. Table 4.1 shows some tested key performance data of the laser.

More details about how the laser works can be found in Michael Ross's dissertation [5].

4.2 Optical Setup

Optical components in the DHI setup include several turning mirrors, a beam expander, three beamsplitters, and some neutral-density (ND) filters. A list of important parts in the optical setup is available in Table 4.2.

Table 4.2: Selected Parts in Optical Setup

Subassembly	**Part**	**Notes**
1st stage turning mirrors	Thorlabs NB1-K13 Thorlabs KM100CP	1-inch mirror mirror mount
Beam expander	CVI Optics PLCC-25.4-28.5-C-1064/532 CVI Optics PLCX-50.8-180.3-C-1064/532 Thorlabs SM1L03 Thorlabs SM2V15	plano-concave lens plano-convex lens input lens' tube output lens' tube
Beamsplitters	3-inch beamsplitter Thorlabs KS3	model unknown mirror mount
2nd stage turning mirrors	Thorlabs PF20-03-G01 Newport GM-2	2-inch mirror mirror mount
Camera ND filters	Thorlabs NE2R40A Thorlabs SM2NFM2	ND 4.0 filter camera adaptor

Upstream from the beam expander, two turning mirrors are used to transmit the beam from the laser onto the optics table on the -x side of Z pinch. The mirrors are AR-coated at the laser wavelength. The mirrors have enough damage threshold to withstand the laser

energy. Fig. 4.1 shows a picture of -x side optics table.

The beam expander is Galilean, using one plano-concave lens and one plano-convex lens. Unlike a Keplerian beam expander, a Galilean beam expander never concentrates the laser beam to a tiny point. This is to avoid extreme laser power concentration that might ionize air and disturb the beam. The focal lengths of the lenses are -50 mm and 350 mm respectively. The lenses have anti-reflective (AR coating on them to reduce the possibility of reflecting laser light back to the laser unit. The lenses are oriented so that their flat surfaces face inside the beam expander to minimize spherical aberration. The lens separation (d) is calculated by

$$d = f_1 + f_2. \tag{4.1}$$

Two lenses are placed about 300 mm apart from each other, as if the plano-convex lens is refracting a diverging beam emitted at about 350 mm away. Some fine adjustment on lens separation is needed, so that the laser beam remains well collimated after the beam expander. The magnification of the beam expander is calculated by

$$m_{12} = -f_2/f_1 \text{ [27]}, \tag{4.2}$$

which yields a magnification of about 7 and an output beam diameter of about 35 mm . When setting up the beam expander, the laser beam has to be well centered on the input (plano-concave) lens, so that the laser line is not significantly turned by the lens.

Three beamsplitters split the beam into two scene beams and two reference beams. The beamsplitters along with their optical mounts have to be large enough to avoid blocking any beam. Two-inch turning mirrors are used to direct the beams across the vacuum chamber to +x direction. The scene beam travels through rectangular windows on the vacuum chamber.

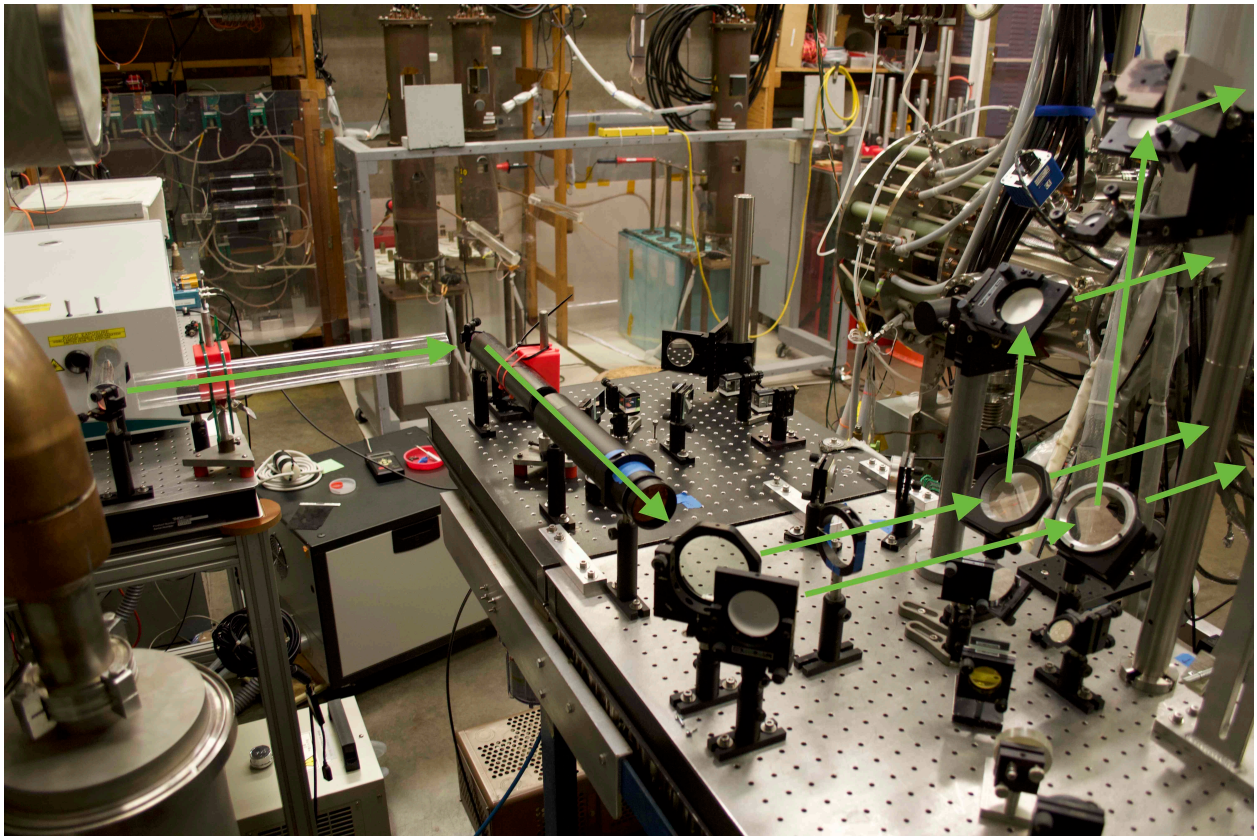

Figure 4.1: DHI setup on -x side optics table. Laser beam is expanded by the beam expander. The beam is then split into two scene beams and two reference beams, directed across the vacuum chamber to +x direction. Some other optical components on the optics table are not part of the DHI setup.

On the +x side optics table, shown in Fig. 4.2, four two-inch turning mirrors are used to direct the scene beam to final turning mirror. Reference beam travels directly to the final turning mirror. The final turning mirrors are large and not off-the-shelf. The final turning mirrors are mounted on some coarse adjustable surface, directing both beams into the camera.

The scene beam and the reference beam are slightly misaligned. In practice, the scene beam mirrors and reference beam mirrors are placed in the one plane perpendicular to the

pinch axis. The reference beam turning mirror is angled to pass the beam just next to the upper scene beam turning mirror. The reference beam turning mirror, the final turning mirror, and the camera is positioned and fixed first. Then, the upper scene beam turning mirror is adjusted to project the scene beam on the camera sensor as well. A crosshair is helpful in overlapping scene beam and reference beam onto the camera sensor.

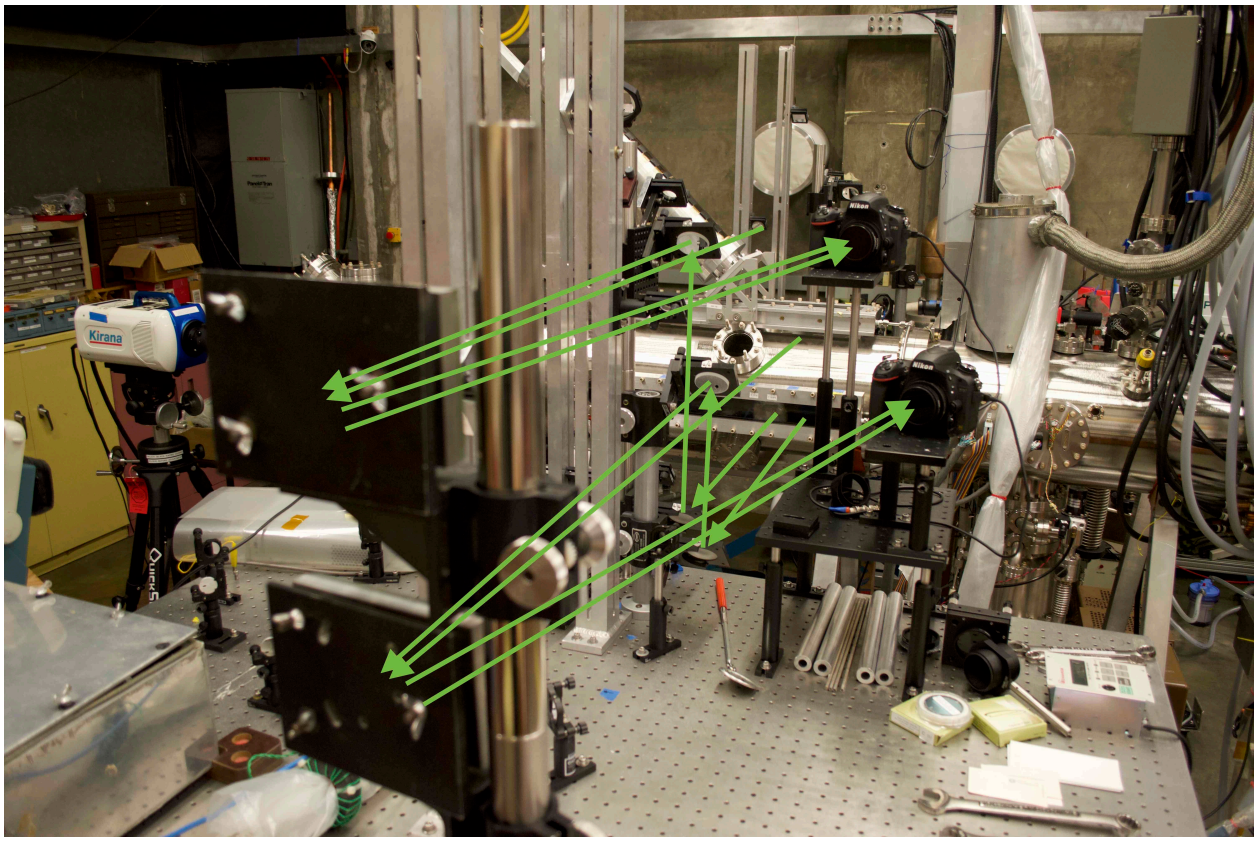

Figure 4.2: DHI setup on +x side optics table. Scene beams travel from the vacuum chamber, and are raised to the same level as reference beams. Reference beams travel above the vaccum chamber and pass near the scene beam turning mirrors. Both beams are directed to the camera with a misalignment angle between them. Some other optical components on the optics table are not part of the DHI setup.

The cameras should have ND filters attached. ND 4.0 filters are used in this experiment,

so that ambient light is mostly blocked, and laser light cannot damage the camera sensor.

4.3 Camera Setup

Two Nikon D750 digital single-lens reflex (DSLR) cameras are used to observe two chords of laser beam. The cameras are mounted on optical posts and breadboards to improve stability and reduce noise. The camera has a 35.9 mm by 24 mm CMOS sensor and an image size of 6016 by 4016 pixels [28]. The camera shutter is left open for the entire duration of the plasma shot. In this thesis, the camera exposure time is 1.3 s, and ISO is set to 100. ISO 100 seems to be the native ISO of this camera sensor. Non-native ISO offers no benefit to DHI. The actual interferometry gate time depends on laser pulse duration, which is about 1.9 ns in this experiment. The cameras are placed in landscape orientation in this thesis, observing more length in the axial direction but less length in the radial direction. More discussion about camera orientation is available in the Chapter 5. Table 4.3 provides a summary of camera specifications and photography parameters.

Table 4.3: Key Specifications of Nikon D750 Camera and Photography Parameters

	Value	**Notes**
Sensor size	35.9 × 24 mm	
Image size	6016 × 4016	∼ 3:2 aspect ratio
Pixel size	∼ 5.97 µm	
Camera ISO	ISO 100	
Interferometry gate time	1.9 ns	Laser pulse duration

Chapter 5

EXPERIMENTAL RESULTS AND DISCUSSION

Again, DHI can measure electron density over some area at an instant of time. Two chords of DHI can form a combined together larger field of view about the pinch. Then, the results from DHI and some other diagnostics can form a combined figure to help us better understand the plasma, such as shape, density, and instability in the pinch. Note that shots presented in this thesis are obtained with 9 kV acceleration capacitor voltage, 7 kV compression capacitor voltage, and 20 µs compression delay.

5.1 Electron Density Measurement

An example from shot 230726054, where the laser was triggered at T+60 µs. DHI code starts with these two photos in Fig. 5.1 as input.

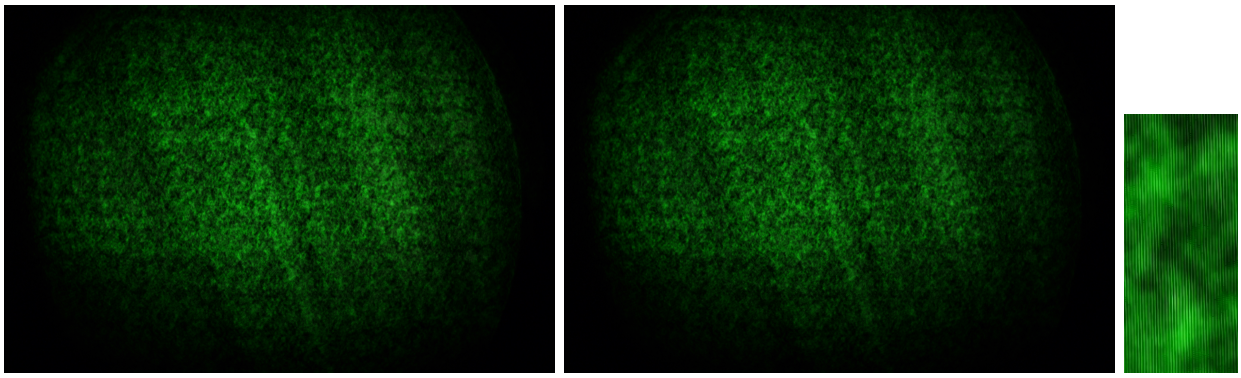

Figure 5.1: An example of photos taken at P7 (a) DHI plasma shot 230726054. (b) DHI baseline shot 230726051. (c) A zoomed-in view on near the center of first photo showing fringes.

There was some plasma disruption at about 28 µs, shown in Fig. 5.2 with magnetic probe data and plasma current data. The magnitude of plasma current and all magnetic probes nearby fluctuated. The gate instant of DHI is represented by a vertical line in the plot.

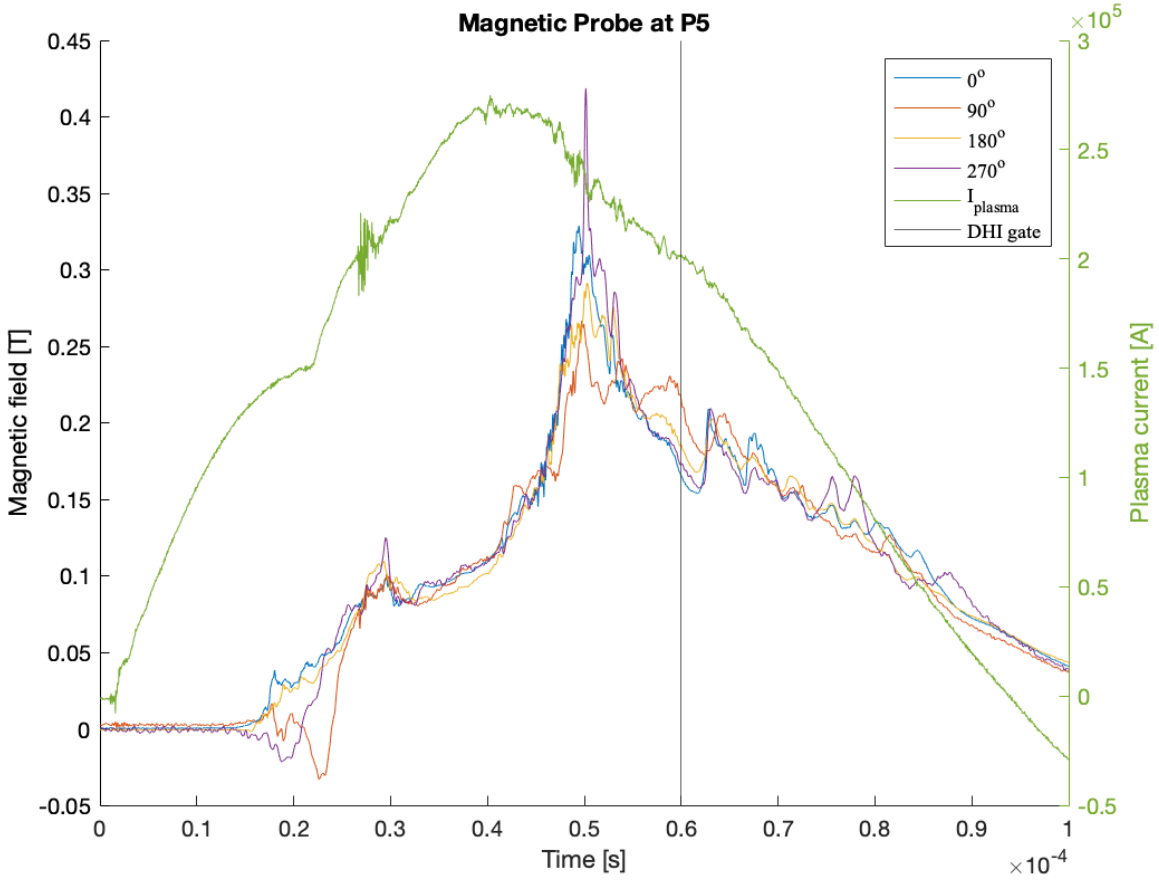

Figure 5.2: Magnetic probe array data at P5 and plasma current of shot 230726054. All signals here fluctuated at about 28 µs, where there was some plasma disruption. The vertical line indicates DHI gate instant.

Holographic reconstruction is performed at some specified reconstruction distance. In this example, the reconstruction distance is 1.3 m. Phase on the reconstruction plane is shown in Fig. 5.3. Zeroth-order (center) and first-order images (left and right) are obvious. A first-

order image is selected for further processing. The coordinate system on the reconstruction plane can be established with pixel size defined by Eq. 3.27.

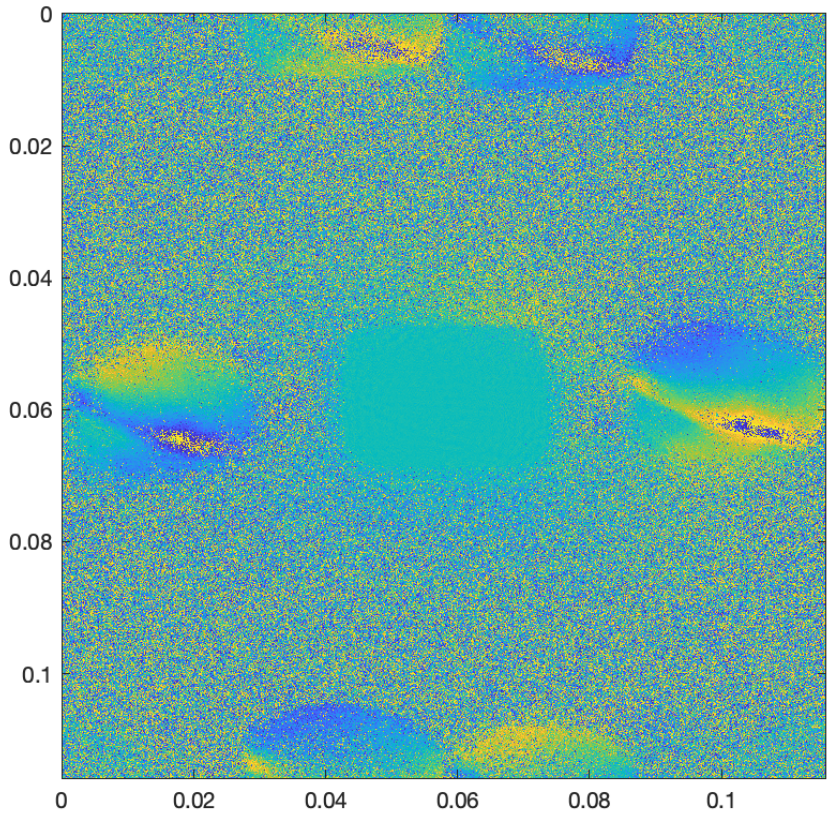

Figure 5.3: Example of holographic reconstruction from shot 230726054 at P7. Both axes are in meter. Color corresponds to phase on the reconstruction plane. Reconstruction distance = 1.3 m. Zeroth-order (center) and first-order images (left and right) are shown. A first-order image is selected for further processing.

The selected first-order image is smoothed and unwrapped. Fringe jumps are recognized and 2π phase shifts are added across fringe jumps. The unwrapped first-order image is directly proportional to the line-integrated density, shown in Fig. 5.4. Note that this figure

has its y-axis flipped. Impact parameter is the distance from central axis. Axial distance is again the distance from the nosecone.

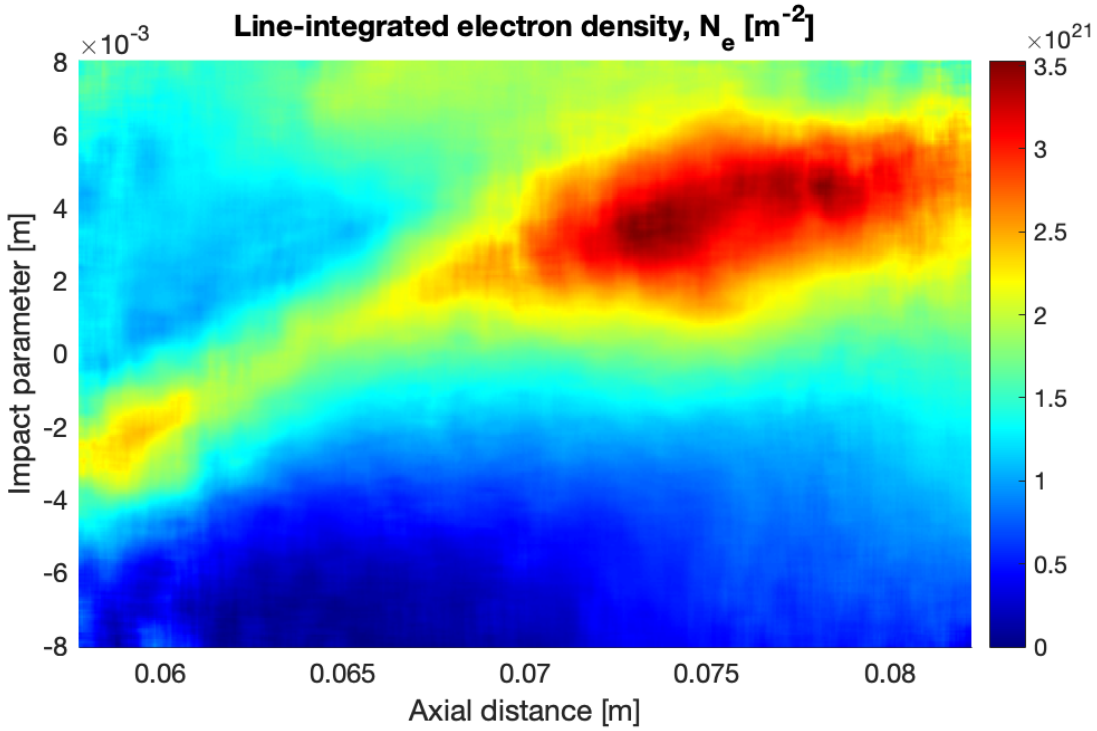

Figure 5.4: Example of line-integrated electron density from shot 230726054 at P7. Impact parameter is the distance away from central axis. Axial distance is again the distance downstream from the nosecone. This figure is further processed to estimate electron number density.

Abel inversion is then applied at each axial locations of line-integrated density profile. For each axial location, two Abel inversions are possible: one in the upper region and one in the lower region. To minimize the difference between two Abel inversion results, Abel inversion

is attempted on a small range of assumed centroid points, near the point of maximum line-integrated density. The optimal centroid for number density is found.

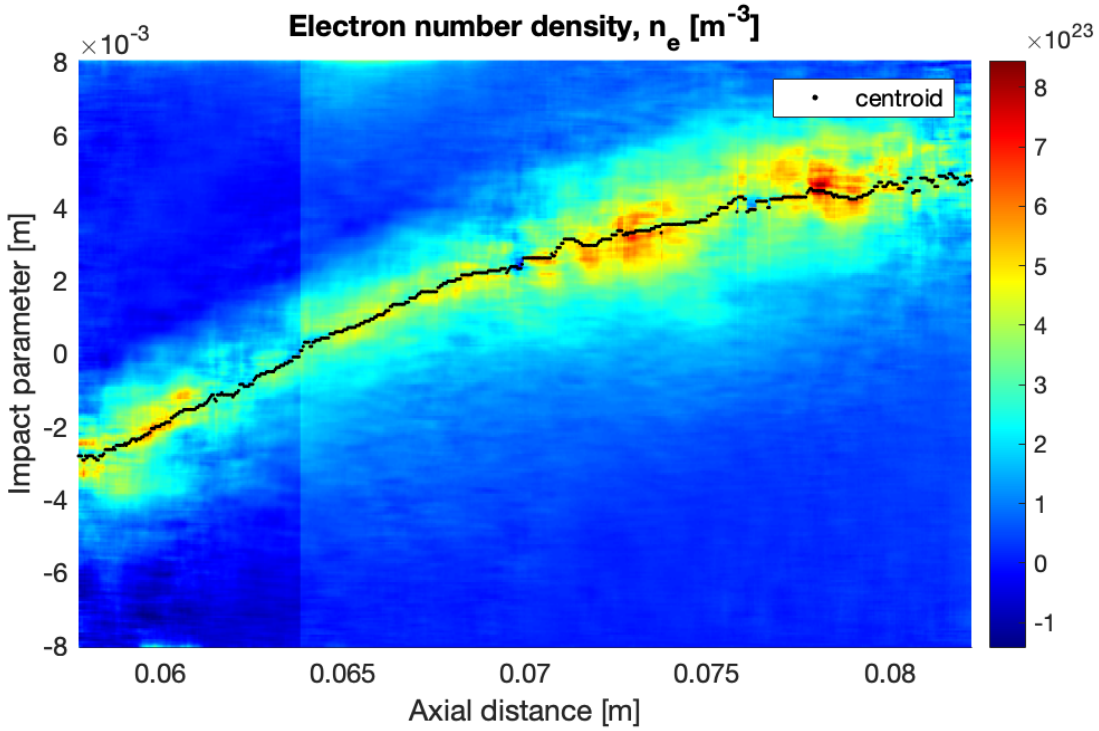

Figure 5.5: Example of electron number density from shot 230726054 at P7. Some axial variation in density can be seen, showing some signs of $m = 0$ instability. The pinch kinks away from the central axis, showing some signs of $m = 1$ instability.

In Fig. 5.5, the DHI data shows both some $m = 0$ instability and some $m = 1$ instability. Plasma density of varies along axis, showing some signs of disjointing. For example, plasma has higher density around P7.3 and P7.7 but lower density near P7.5. The pinch deviates from the machine axis slightly, with maximum deviation of about 5 mm in the figure near

P8. Note that the maximum number density on the figure may not be very accurate. Abel inversion can have a relatively large error near the density centroid [16].

5.2 Comparing DHI Density Profile to Pinch Current Centroid

Fig. 5.6 and Fig. 5.7 show shot 230726054 at T+60 µs plotted with line-integrated density and number density.

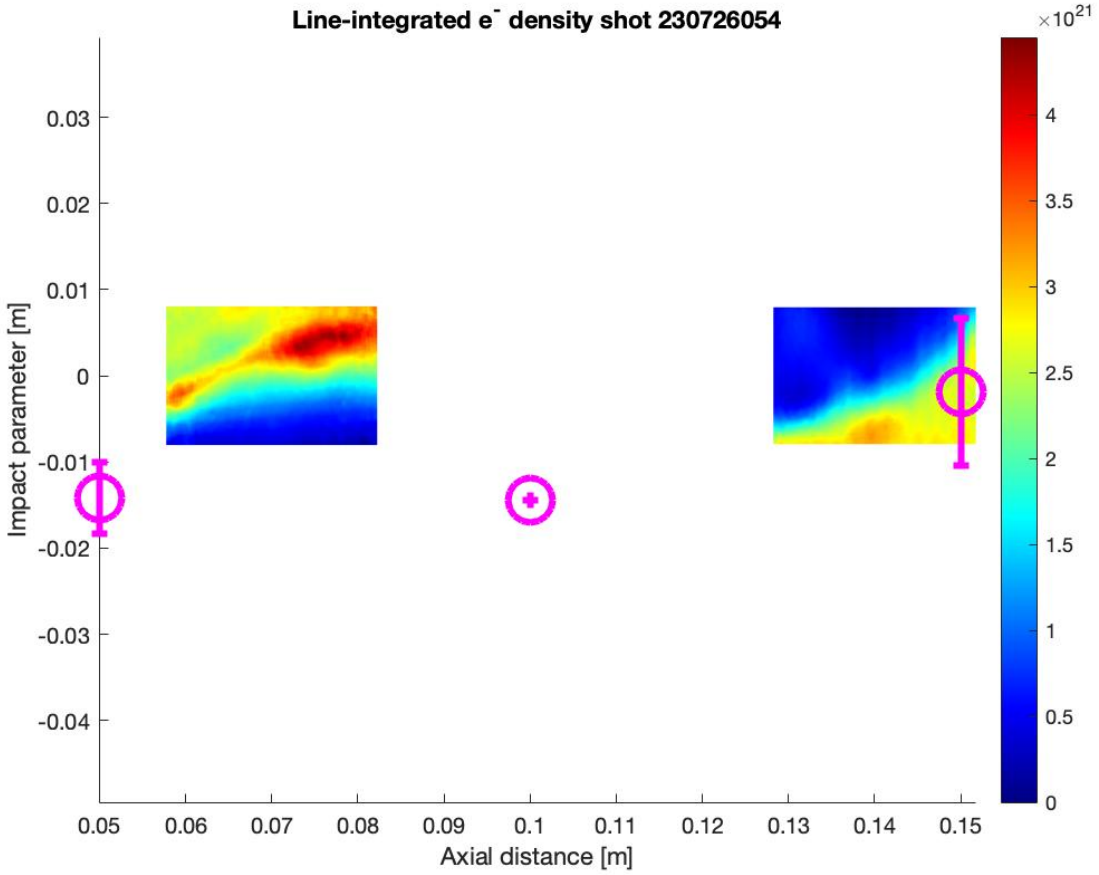

Figure 5.6: Shot 230726054 at T+60 µs with line-integrated density. Axes are in meter. Magenta circles show the estimated pinch current centroid from magnetic probes with statistical error at three axial locations. The pinch appears to drift over of the view of DHI near P14. There is some agreement between DHI results and estimated pinch current centroid.

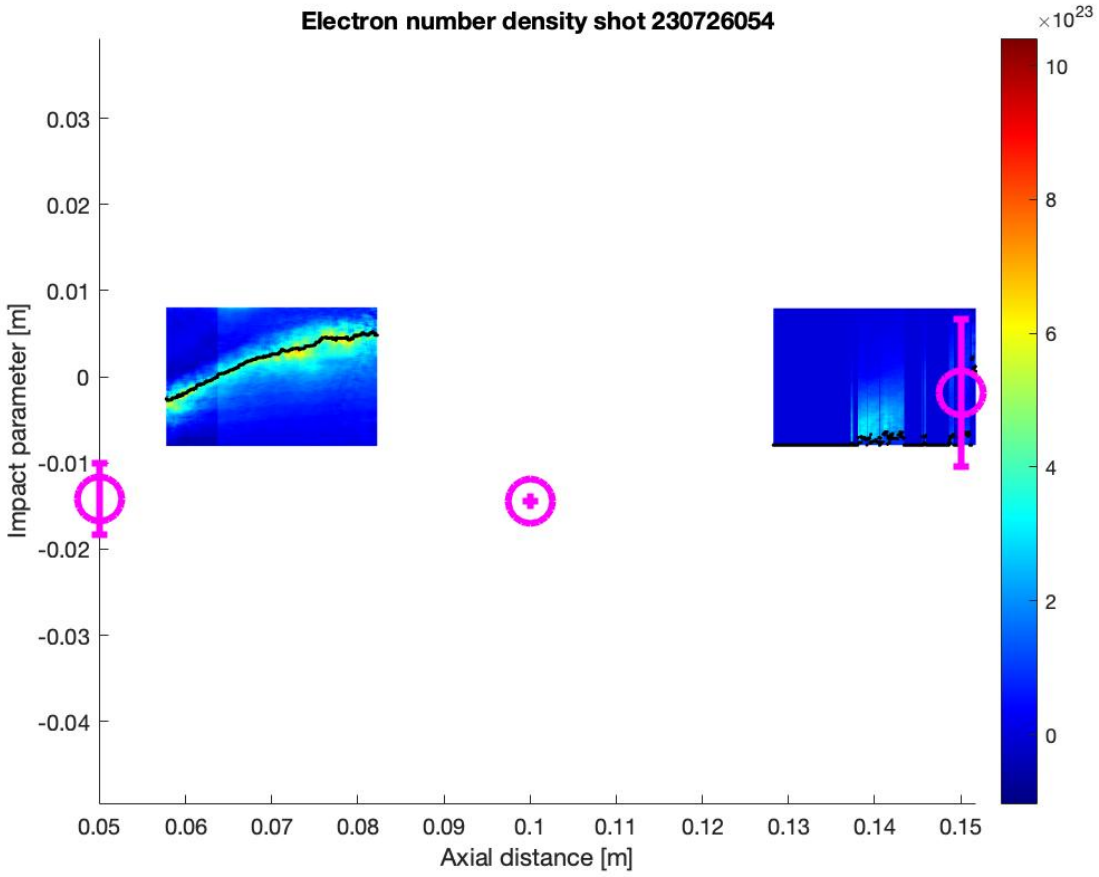

Figure 5.7: Shot 230726054 at T+60 µs with number density. Axes are in meter. Magenta circles show the estimated pinch current centroid from magnetic probes with statistical error at three axial locations. Abel inversion cannot resolve near P14 because pinch center is our of view. There is some agreement between DHI results and estimated pinch current centroid.

Pinch current centroid can be estimated from magnetic probe data using Ampere's Law. This is done by minimizing the difference between B-field due to estimated current centroid and measured B-field. Some comparison can be made between centroid of density profile and pinch current centroid. Results from two chords of DHI and pinch current centroid are plotted together. Pinch current centroids estimated from magnetic probe data are represented as

magenta circles with statistical error bars at various axial locations. The statistical error of estimated centroid at P10 is small because there were limited magnetic probe data available and the optimization process always fits the available data.

Fig. 5.8 and Fig. 5.9 show shot 230726036 at T+50 µs with line-integrated density and number density.

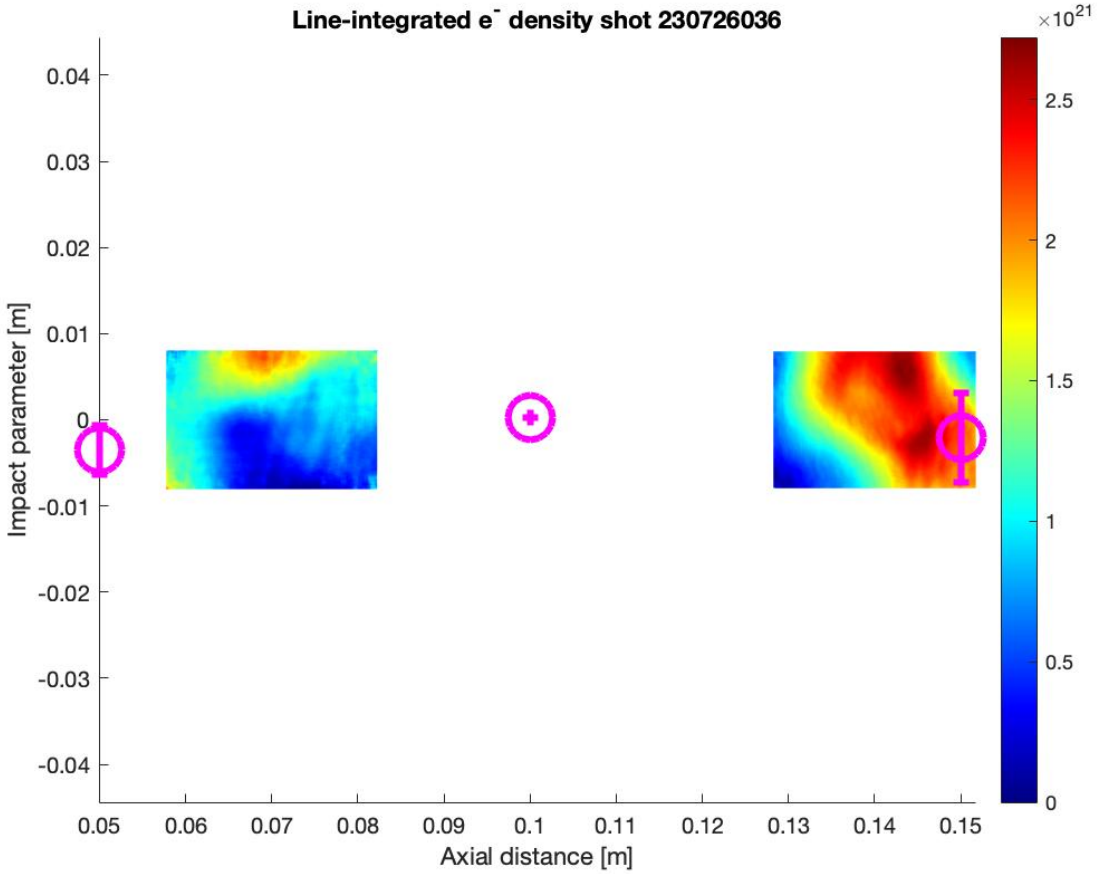

Figure 5.8: shot 230726036 at T+50 µs with line-integrated density. Magenta circles show the estimated pinch current centroid from magnetic probes with statistical error at three axial locations. The pinch is not clearly captured the DHI chords here. There is some agreement between DHI results and estimated pinch current centroid.

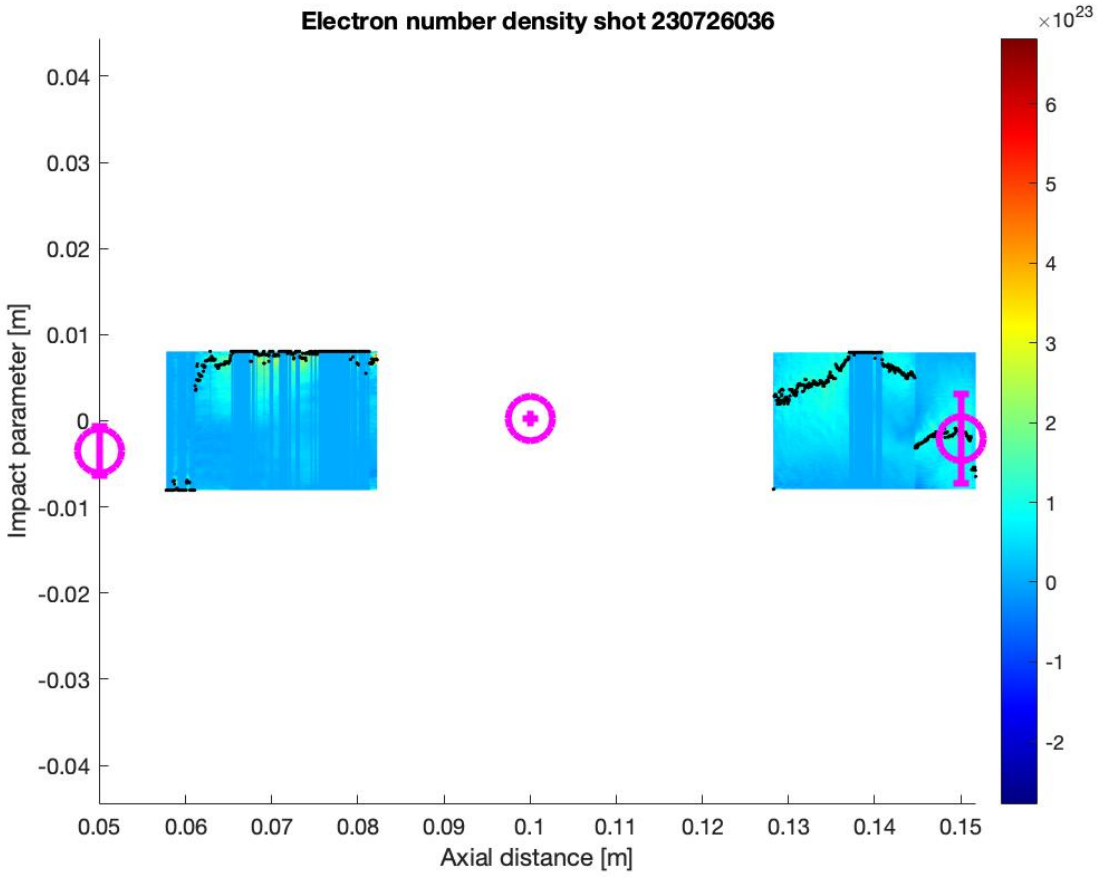

Figure 5.9: shot 230726036 at at T+50 µs with number density. Magenta circles show the estimated pinch current centroid from magnetic probes with statistical error at three axial locations. There is some difficulty in resolving number density with Abel inversion because the pinch is not clearly captured. There is some agreement between DHI results and estimated pinch current centroid.

DHI has a high spatial resolution, allowing it to more accurately measures the location of the pinch. DHI has a relatively small field of view. Magnetic probe arrays can estimate location of the pinch current centroid widely but with some uncertainty. It can be difficult for a DHI chord to capture the pinch due to limited view of the chord. If the DHI chord

does not intersect with the pinch, electron number density most likely cannot be resolved by Abel inversion.

The examples show some agreement between density profiles and pinch current centroids. Ideally, estimated pinch current centroids would overlap with density profile centers. The examples also show that the pinch often moves out of the view of a DHI chord. It might be difficult to obtain a clear view of the pinch in landscape camera orientation, where the sensor size corresponding to radial direction is merely 24 mm.

5.3 Signal Noise

Holographic reconstruction can be applied on two baseline photos to determine signal noise. Among collected data, the result shows some noise with line-integrated density that peaks at about 10^{21} to 2×10^{21} m^{-2}. The plasma probably has a relatively low electron density far away from the nosecone, for example, at about P40. From magnetic probe data, plasma is usually less stable there, and pinch current is less than what is near the nosecone. Plasma has more longitudinal distance to build up disturbance as well, which might explain why electron density there is lower. The density is close to the noise level of current DHI method. Therefore, it is difficult to use DHI to measure electron density far away from the nosecone. Also, Jared Smythe suggested that the electron number density in the extension region is about 10^{20} m^{-3}, which is too low to measure with DHI [17].

It is highly recommended to have beam path enclosed to reduce shot-to-shot variation in hologram due to air currents. Without beam guide, noise due to air currenst can fully disturb phase change due to pinch plasma. Beam path was only partially covered by pipes in the data collected in this thesis. Michael Ross suggested that the peak noise is about 10^{21} m^{-2} if there is good beam path coverage. In the DHI setup, the most important portion of beam path to enclose is on the -x side [5].

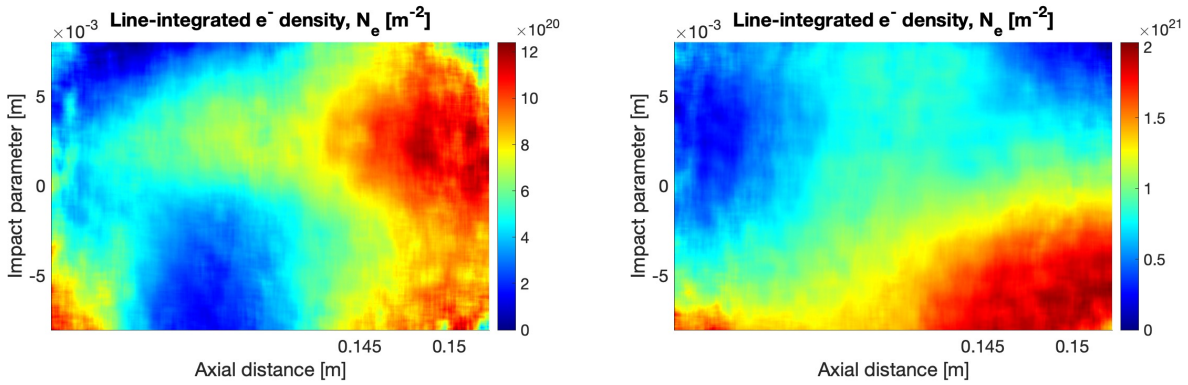

Figure 5.10: Examples of DHI baseline noise level from: (a) shot 230726012 compared to shot 230726009. (b) shot 230726055 compared to shot 230726051. There is some noise that peaks about 10^{21} to 2×10^{21} m^{-2} in the data collected in this thesis.

Shots presented in the thesis are verified by attempting holographic reconstruction with respect to two baselines. Both reconstructions result in similar shapes. So their results are much less likely to be pure noise, but there are some actual signals.

5.4 Suggested Improvement

Nikon D750 camera has a sensor size of 35.9 mm by 24 mm [28]. This sensor is larger than the current 35-mm-wide laser beam. The beam cannot fully illuminate the entire sensor. Also, any slightly sub-optimal arrangement of the beam expander, mirrors, lenses, and beamsplitters on the beam path is likely to further reduce the illuminated area on the sensor. Only a portion of the sensor is actually used to observe the plasma. To fully use the sensor area, the beam diameter has to be further expanded: at least 43.2 mm to cover the diagonal of the sensor. Assuming a new beam diameter of 43.2 mm, a new beam expander with a magnifying power greater than 7.81 is needed. To accommodate larger laser beam, larger mirrors and potentially larger beamsplitters are needed. On turning mirrors, 3 inch is a convenient size to find off-the-shelf products. On beamsplitters, the required size depends

on whether their optical mounts are wide enough to avoid blocking incoming and outgoing beams.

Consumer digital cameras with larger sensor area, for example some medium format sensors, and sufficiently small pixel size are available off-the-shelf. With a sufficiently large beam diameter, and sufficiently high power density of the expanded beam, a larger sensor cam improve field of view in the vacuum chamber.

It is possible to cover even more area in the vacuum chamber without changing camera sensor by expanding and shrinking the laser beam. The laser beam can be expanded larger then the camera sensor area and travel though the pinch. The upper limit in this experiment is the size of rectangular viewing port. Before directing the laser beam into the camera, the beam has to shrink down so that a large portion of the beam can fit in the sensor. Note that this decreases the actual spacial resolution of the DHI setup, and some small details in the plasma may not be resolved.

More chords can be added to the DHI setup to further expand the combined field of view. Adding chords is relatively easy, by simply adding more bemasplitters, mirrors, and cameras. Two neighboring chords are spaced with some gap between due to bemasplitter arrangement. The gap in current setup is about 7 cm, which can be reduced by using rectangular bemasplitter and edge-less optical mounts. Adding more chords are helpful up to a point downstream where plasma density is low and cannot be measured by DHI.

It might be difficult to capturing the pinch with DHI field of view. It is recommended to prioritize capturing the pinch other than looking for more field of view in axial direction. Unless the laser beam is cropped by the vacuum chamber rectangular window, it is recommended to place the camera sensor in portrait orientation, to improve field of view in radial direction.

It is recommended in general to mis-align scene beam and reference beam so that the interference fringes are parallel to the long side of the camera sensor. Thus, in holographic reconstruction, the first-order image can sit next the long side of the zeroth-order image, reducing the reconstructing distance required to separate two images. Shorter reconstruction

distance improves spatial resolution on density measurement, as suggested by Eq. 3.27.

Despite the fact that the image size of consumer digital cameras has not increased very significantly over the past decade, DHI can still benefit from using contemporary (2023) CPU with more computing power. The computer time required to process DHI hologram is strongly related to the size of first-order image. On a 2017 low-power laptop CPU, processing a DHI holograms with full-resolution first-order image can take more than 20 minutes, with the majority of time spent on Abel inversion. Performing Abel inversion on an image at full resolution involves solving more than 10^3 linear systems. The number of linear systems depend on how many attempts are made to find best centroid of number density. Each linear system features triangular matrices whose sizes are about 10^3. In this thesis, Abel inversion is performed at a reduced resolution to save computer time. With a 2023 desktop CPU, processing DHI holograms at full resolution can take much less time.

Chapter 6

SUMMARY AND CONCLUSION

Fusion power can potentially power human civilization with clean energy and has a huge advantage in deep space propulsion. Static Z-pinch devices suffer from instabilities that limited their fusion confinement performance. The SFS Z-pinch concept can potentially work as a fusion power generator and a space propulsion engine. Measurement of plasma parameters, like density, are important for fusion confinement research. ZaP-HD is the second device in our lab to study SFS Z-pinch plasma. A suite of diagnostics available at ZaP-HD at discussed.

DHI method featuring Fresnel transform is reviewed. The equipment applied to set up two-chord DHI at ZaP-HD is described. The DHI setup measures instantaneous electron density over some area near the nosecone, revealing the structure of the pinch there. The measurement shows a maximum electron density of more than 10^{23} m^{-3}. The setup expands our combined field of view on the pinch. Pinch current centroid can be estimated from magnetic probe array using Fourier expansion or optimization, with some spatial uncertainty. Comparison between DHI results and estimates from magnetic probe arrays shows some agreement on the plasma centroid. Along with other diagnostics, 2-chord DHI helps us better understand the overall structure of the pinch. Pinch current centroids estimated from magnetic probe array shows some agreement with DHI data. Field of view of the DHI setup can be further improved with better camera orientation, larger laser beam diameter, and larger camera sensor. Combined field of view of DHI can be further expanded by adding more chords, which can be done relatively easily. In general, larger field of view can improve our understanding about overall pinch structure. In agreement Michael Ross's finding, DHI setup has some baseline noise that peaks at about 10^{21} m^{-2} line-integrated electron density,

and covering the beam path to block air current is the key in reducing baseline noise to this level. A modern (as of 2023) desktop CPU can greatly save time in calculating Abel inversion.

BIBLIOGRAPHY

[1] Reinhard Beer and Fredric William Taylor. The abundance of ch3d and the d/h ratio in jupiter. *The Astrophysical Journal*, 179:309–328, 1973. https://doi.org/10.1086/151870.

[2] U. Shumlak et al. Advanced space propulsion based on the flow-stabilized z-pinch fusion concept. In *42nd AIAA/ASME/SAE/ASEE Joint Propulsion Conference & Exhibit*, page 4805, 2006. https://doi.org/10.2514/6.2006-4805.

[3] Andrew S. Richardson. *2019 NRL plasma formulary*. United States Naval Research Laboratory, Washington, D.C., 2019. https://www.nrl.navy.mil/Portals/38/PDF%20Files/NRL_Plasma_Formulary_2019.pdf.

[4] Sehila M. Gonzalez de Vicente et al. Overview on the management of radioactive waste from fusion facilities: Iter, demonstration machines and power plants. *Nucl. Fusion*, 62(8):085001, 2022. https://doi.org/10.1088/1741-4326/ac62f7.

[5] Michael Patrick Ross. *Exploring plasma stability and confinement with high resolution density measurements on the ZaP-HD Flow Z-Pinch*. PhD thesis, University of Washington, 2016. http://hdl.handle.net/1773/38055.

[6] Eleanor Forbes. *Diagnostic Development and Plasma-Material Interaction Studies on the ZaP-HD Device*. PhD thesis, University of Washington, 2020. http://hdl.handle.net/1773/46357.

[7] B.B. Kadomtsev. Hydromagnetic stability of a plasma. *Reviews of Plasma Physics*, 2:153, 1966.

[8] U. Shumlak and C. W. Hartman. Sheared flow stabilization of the $m = 1$ kink mode in Z pinches. *Phys. Rev. Lett.*, 75(18):3285–3288, Oct 1995. https://doi.org/10.1103/PhysRevLett.75.3285.

[9] Uri Shumlak et al. Evidence of stabilization in the Z-pinch. *Phys. Rev. Lett.*, 87:205005, Oct 2001. https://doi.org/10.1103/PhysRevLett.87.205005.

[10] Uri Shumlak et al. Equilibrium, flow shear and stability measurements in the z-pinch. *Nuclear Fusion*, 49(7):075039, Jul 2009. https://doi.org/10.1088/0029-5515/49/7/075039.

[11] Y. Zhang et al. Sustained neutron production from a sheared-flow stabilized z pinch. *Phys. Rev. Lett.*, 122:135001, Apr 2019. https://doi.org/10.1103/PhysRevLett.122.135001.

[12] Uri Shumlak et al. Increasing plasma parameters using sheared flow stabilization of a Z-pinch. *Physics of Plasmas*, 24(5):055702, 02 2017. https://doi.org/10.1063/1.4977468.

[13] Eleanor G. Forbes and Uri Shumlak et al. Progress toward a compact fusion reactor using the sheared-flow-stabilized z-pinch. *Fusion Science and Technology*, 75(7), 7 2019. https://doi.org/10.1080/15361055.2019.1622971.

[14] U. Shumlak. Z-pinch fusion. *Journal of Applied Physics*, 127(20):200901, May 2020. https://doi.org/10.1063/5.0004228.

[15] Elliot L Claveau. *Axial Evolution of a Sheared-Flow-Stabilized Z Pinch*. PhD thesis, University of Washington, 2020. http://hdl.handle.net/1773/46361.

[16] Michael Patrick Ross and Uri Shumlak. Digital holographic interferometry employing fresnel transform reconstruction for the study of flow shear stabilized z-pinch plasmas. *Rev. Sci. Instrum.*, 87(10):103502, 2016. https://doi.org/10.1063/1.4964387.

[17] Jared Smythe. Electrode geometry effects on plume characteristics and thruster performance of zap-hd. Master's thesis, University of Washington, 2023. https://www.proquest.com/dissertations-theses/electrode-geometry-effects-on-plume/docview/2839000115/se-2.

[18] Amierul Aqil bin Khairi. Graphite electrode characterization on the zap-hd sheared-flow-stabilized z-pinch device. Master's thesis, University of Washington, 2021. http://hdl.handle.net/1773/47909.

[19] R. P. Golingo. Modeling magnetic fields measured by surface probes embedded in a cylindrical flux conserver. *Review of Scientific Instruments*, 78(3):033504, 03 2007. http://doi.org/10.1063/1.2713435.

[20] E. G. Forbes and U. Shumlak. Spatio-temporal ion temperature and velocity measurements in a Z pinch using fast-framing spectroscopy. *Review of Scientific Instruments*, 91(8):083104, 08 2020. https://doi.org/10.1063/5.0012255.

[21] Sean D. Knecht, Raymond P. Golingo, Brian A. Nelson, and Uri Shumlak. Calculation of the equilibrium evolution of the zap flow z -pinch using a four-chord interferometer. *IEEE Transactions on Plasma Science*, 43(8):2469–2479, 2015.

[22] Timothy Joseph Lloyd. Comparison of diagnostics for determining z pinch centroid in the zap-hd experiment. Master's thesis, University of Washington, 2022. http://hdl.handle.net/1773/48430.

[23] Donald Gary Swanson. *Plasma waves*. Academic Press, Boston, 1989.

[24] Ian H. Hutchinson. *Principles of plasma diagnostics*. Cambridge University Press, Cambridge, 1987.

[25] Thomas Kreis. *Handbook of Holographic Interferometry: Optical and Digital Methods*. Wiley, Germany, 2005.

[26] EKSPLA. *NL121 Series Laser Technical Description & User's Manual*. Lithuania, 2014.

[27] Thorlabs. Does it matter whether a beam expander or reducer has a keplerian or galilean design? https://www.thorlabs.com/newgrouppage9.cfm?objectgroup_id=14648.

[28] Nikon. *Digital Camera D750 User's Manual*, 2014. https://download.nikonimglib.com/archive3/zfZiH00gS82A04CSS4P024qk3H46/D750FM_DL(En)05.pdf.

Appendix A

PHOTO GALLERY OF THE DHI SETUP

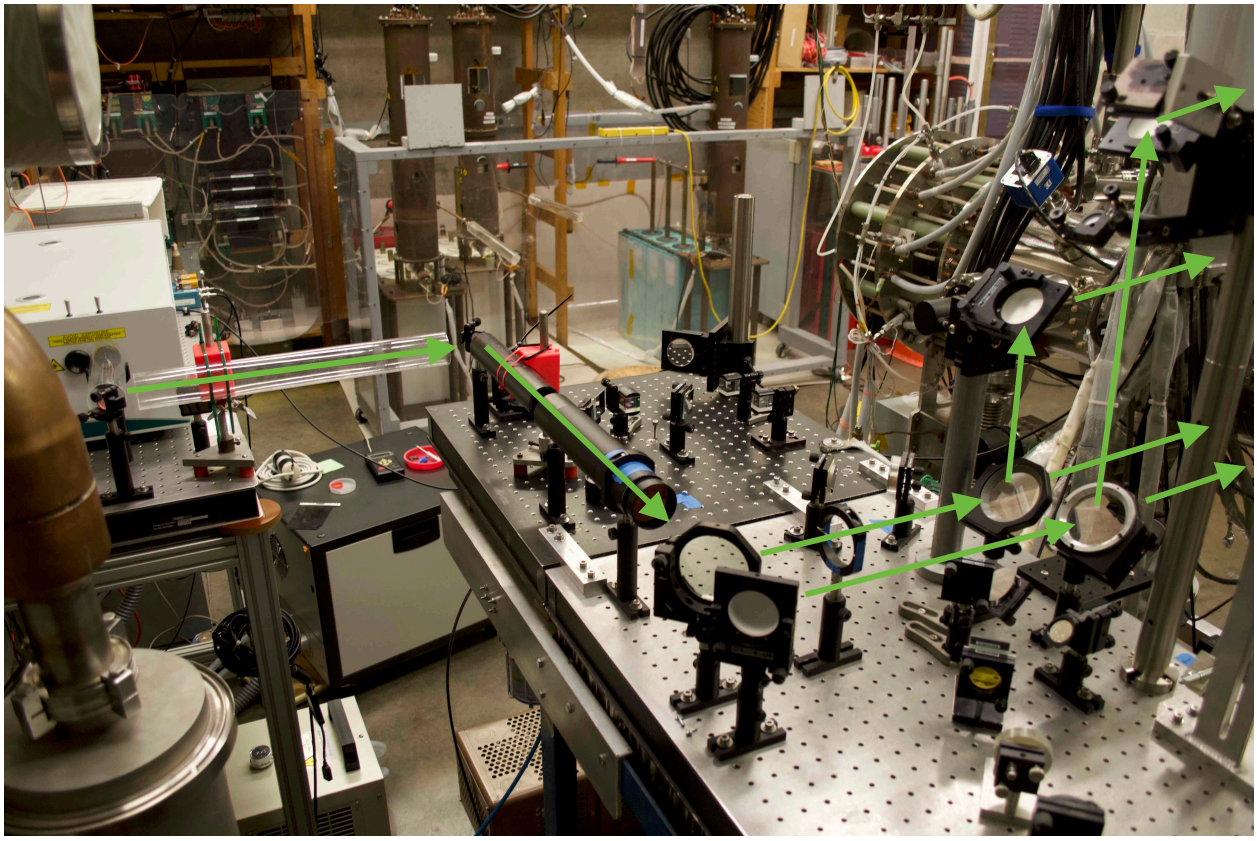

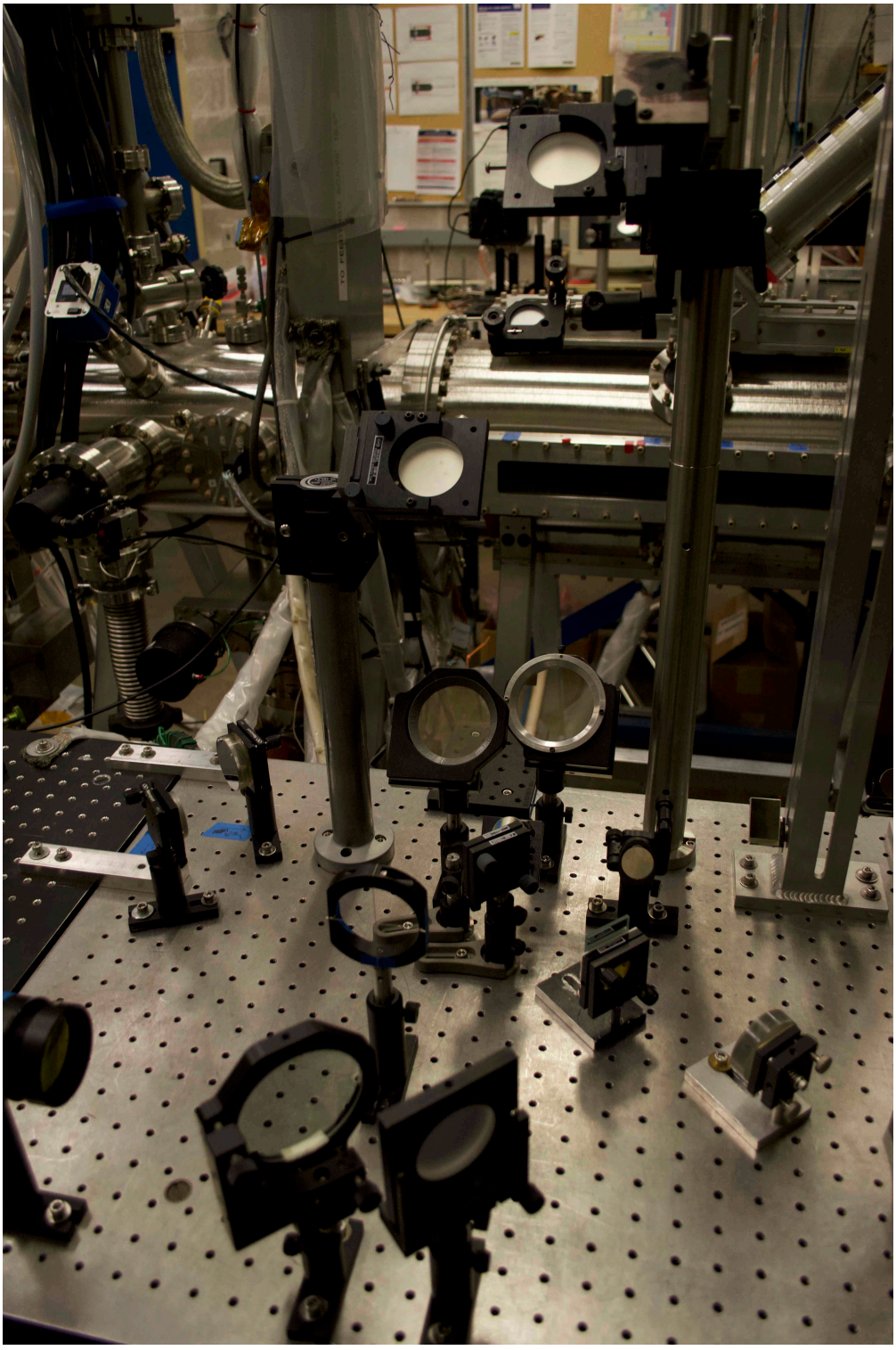

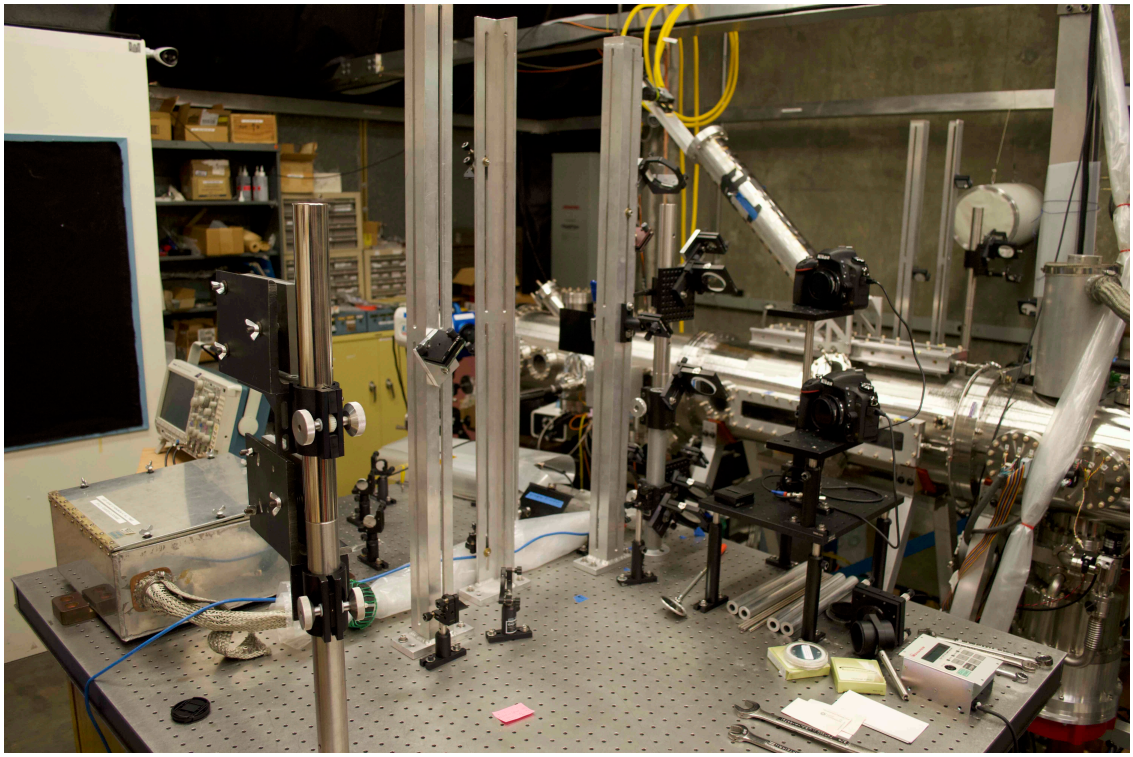

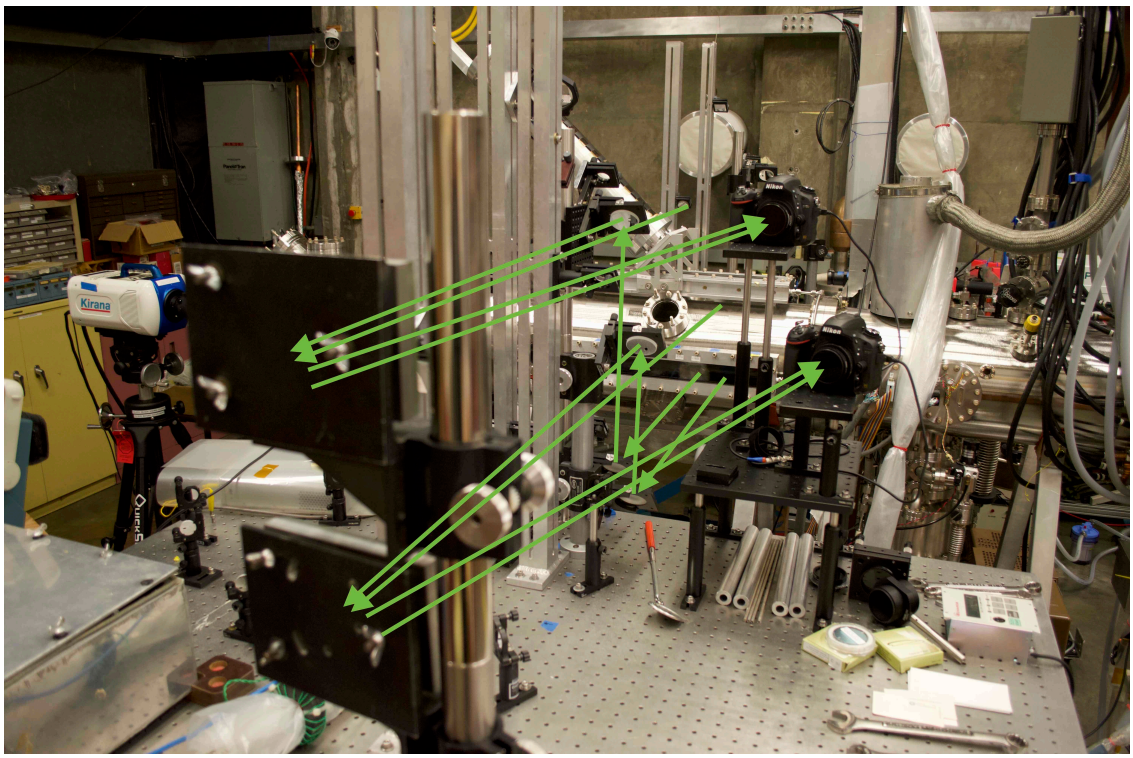
Kirana

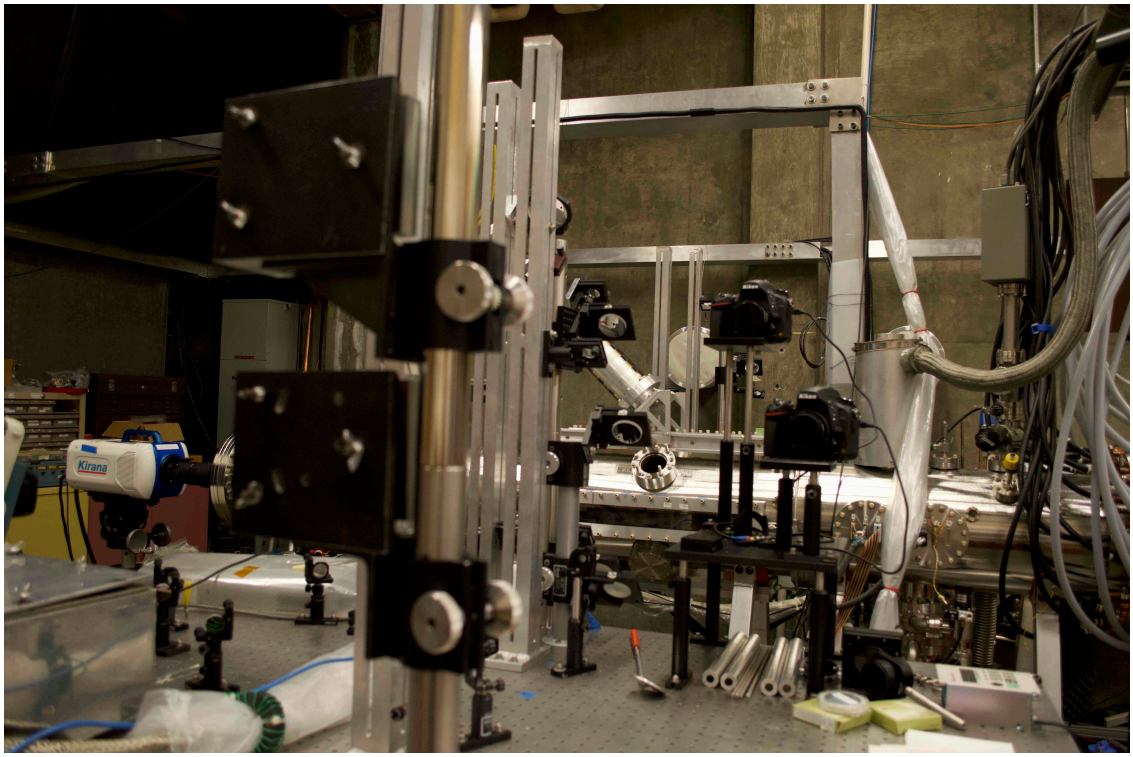
Kirana

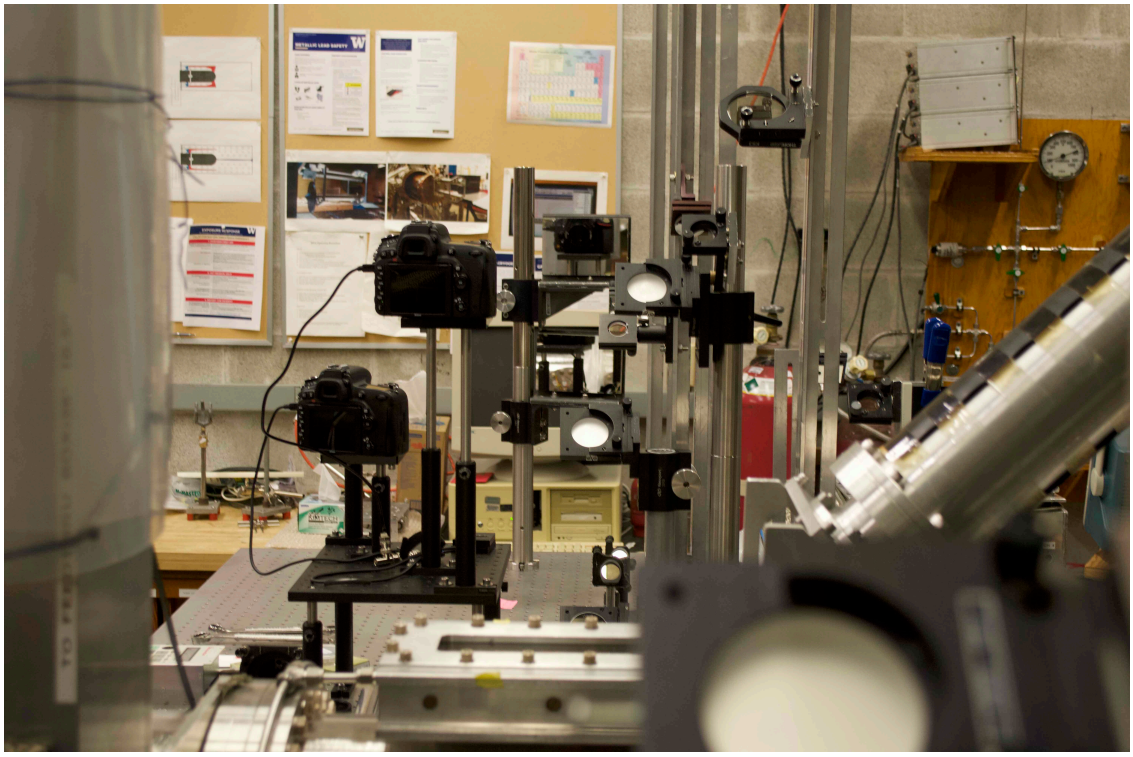

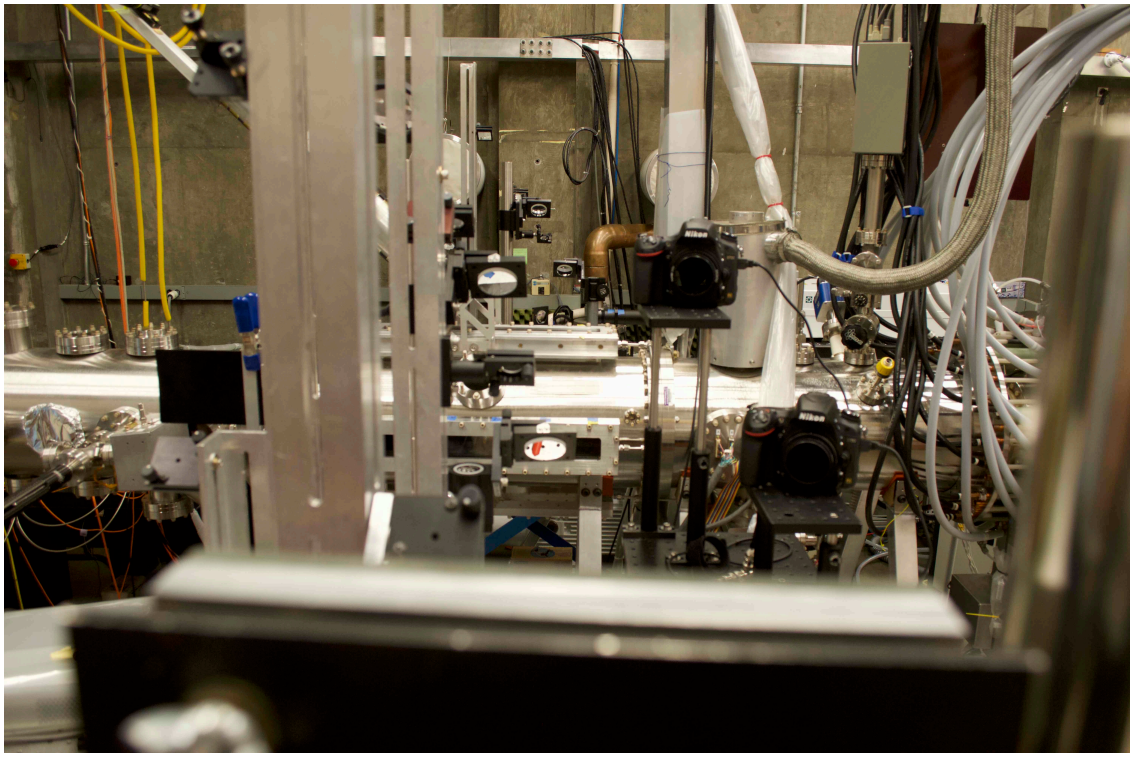

Appendix B

LIMIT OF DHI RESOLUTION

In DHI using Fresnel transform, if we assume that an experimentalist is capable of setting any misalignment angle, then what is the limit of resolution in radial direction?

Let's consider a camera senor with square pixel of size Δx. The sensor has a image size of M by N, where $M \leq N$. Then, the aspect ratio of the sensor is $r = N/M \geq 1$, and the physical size of the sensor is $M\Delta x$ by $rM\Delta x$. The laser used in this DHI setup has the wavelength λ.

To maximize resolution in radial direction, orient the sensor so that the long side is in the radial direction, and misalign scene beam and reference beam so that interference fringes are parallel to the long side. Let's assume that no pixel is trimmed near the edge of the photo during post-processing. And of course let's assume that the entire sensor is covered by the interference pattern.

As mentioned previously, the reconstruction plane has spatial size

$$\frac{d\lambda}{\Delta x} \times \frac{d\lambda}{\Delta x}.$$

The zeroth order image and first order image has spatial size

$$M\Delta x \times rM\Delta x.$$

A first order image therefore occupies a portion of the reconstruction plane

$$\frac{M\Delta x}{d\lambda/\Delta x} \times \frac{rM\Delta x}{d\lambda/\Delta x}.$$

The pixel count on a first order image is then

$$\frac{M\Delta x}{d\lambda/\Delta x}M \times \frac{rM\Delta x}{d\lambda/\Delta x}rM,$$

or alternatively written

$$\frac{M^2\Delta x^2}{d\lambda} \times \frac{r^2 M^2 \Delta x^2}{d\lambda}.$$

The misalignment angle θ should be optimized to reduce reconstruction distance d, so that pixel count on the first order image is large. Thus, resolution in radial direction can be optimized.

Let's consider some limiting factors on the reconstruction distance d:

- A first order image must be sufficiently separated from the zeroth order image so that they do not overlap;

- A first order image can only occupy a sufficiently small portion of the reconstruction plane so that it is not clipped by edges of the reconstruction plane or by the zeroth order image.

Let's consider the first factor. To separate the first order image from the zeroth order image, the center separation h_i must be longer than short side of first order image:

$$h_i = d\tan\theta \geq M\Delta x.$$

To avoid aliasing, the misalignment angle θ must be small enough:

$$\sin\theta = \frac{\lambda}{\delta} \leq \frac{\lambda}{2\Delta x},$$

This puts a limit on minimal reconstruction distance

$$d \geq \frac{M\Delta x}{\tan(\arcsin(\frac{\lambda}{2\Delta x}))}.$$

Without small angle approximation:

$$d \geq \frac{M\Delta x}{\frac{\lambda/(2\Delta x)}{\sqrt{1-(\lambda/(2\Delta x))^2}}}$$

$$d \geq \frac{2M\Delta x^2}{\lambda}\sqrt{1-\left(\frac{\lambda}{2\Delta x}\right)^2}.$$

Pixel count on the first order image becomes

$$\frac{M^2\Delta x^2}{2M\Delta x^2\sqrt{1-\left(\frac{\lambda}{2\Delta x}\right)^2}} \times \frac{r^2M^2\Delta x^2}{2M\Delta x^2\sqrt{1-\left(\frac{\lambda}{2\Delta x}\right)^2}}$$
$$\frac{M}{2\sqrt{1-\left(\frac{\lambda}{2\Delta x}\right)^2}} \times \frac{r^2M}{2\sqrt{1-\left(\frac{\lambda}{2\Delta x}\right)^2}}.$$

With small angle approximation, pixel count simplifies to

$$\frac{M}{2} \times \frac{r^2M}{2}.$$

Again, this is the maximum possible pixel count on the first order image imposing the limiting factor of large enough separation between first order image and zeroth order image.

Let's consider the second factor. To maximize the portion of reconstruction plane occupied by a first order image, place first order image, zeroth order image, and another first order image side by side. Both first order images have one side sitting right on the edge of the reconstruction plane. In the direction of short side, pixel count of a first order image must be less than one third of pixel count of the reconstruction plane:

$$\frac{M^2\Delta x^2}{d\lambda} \leq \frac{M}{3}.$$

The reconstruction distance must be

$$d \geq \frac{3M\Delta x^2}{\lambda}.$$

Pixel count of the first order image becomes

$$\frac{M}{3} \times \frac{r^2M}{3}.$$

In the direction of long side, pixel count limit of a first order image is simply rM.

The limiting factor about sufficiently small first order image is stricter. Usually, a camera sensor has an aspect ratio less than 3. We can conclude that maximum possible pixel count of DHI in radial direction is usually $r^2M/3$.

The conclusion suggests that there is some optimal misalignment angle that maximizes pixel count in radial direction. In the case of maximum possible pixel count, the center separation of first order image is one third of spatial size of reconstruction plane

$$h_i = d \tan\theta = \frac{1}{3}\frac{d\lambda}{\Delta x}.$$

Optimal misalignment angle is

$$\theta = \arctan\frac{\lambda}{3\Delta x}.$$